



CERN-EP-2019 -XXX  
Day Month 2019

# $\Lambda K$ femtoscopy in Pb–Pb collisions at $\sqrt{s_{NN}} = 2.76$ TeV

ALICE Collaboration\*

## Abstract

The first measurements of the scattering parameters of  $\Lambda K$  pairs in all three charge combinations ( $\Lambda K^+$ ,  $\Lambda K^-$ , and  $\Lambda K_S^0$ ) are presented. The results are achieved through a femtoscopic analysis of  $\Lambda K$  correlations in Pb–Pb collisions at  $\sqrt{s_{NN}} = 2.76$  TeV recorded by ALICE at the LHC. The femtoscopic correlations result from strong final-state interactions, and are fit with a parametrization allowing for both the characterization of the pair emission source and the measurement of the scattering parameters for the particle pairs. Extensive studies with the THERMINATOR 2 event generator provide a good description of the non-femtoscopic background, which results mainly from collective effects, with unprecedented precision. Furthermore, together with HIJING simulations, this model is used to account for contributions from residual correlations induced by feed-down from particle decays. The extracted scattering parameters indicate that the strong force is repulsive in the  $\Lambda K^+$  interaction and attractive in the  $\Lambda K^-$  and  $\Lambda K_S^0$  interactions. The results suggest an effect arising either from different quark–antiquark interactions between the pairs ( $s\bar{s}$  in  $\Lambda K^+$  and  $u\bar{u}$  in  $\Lambda K^-$ ) or from different net strangeness for each system ( $S=0$  for  $\Lambda K^+$ , and  $S=-2$  for  $\Lambda K^-$ ). Finally, the  $\Lambda K$  systems exhibit source radii larger than expected from extrapolation from identical particle femtoscopic studies. This effect is interpreted as resulting from the separation in space–time of the single-particle  $\Lambda$  and  $K$  source distributions.

## 1 Introduction

Femtoscopy is an experimental method used to study the space–time characteristics of the particle emitting sources in relativistic particle collisions [1]. With this method, two- (or many-) particle relative-momentum correlation functions are used to connect the final-state momentum distributions to the space–time distributions of particle emission at freeze-out. The correlation functions are sensitive to quantum statistics, as well as strong and Coulomb final-state interactions (FSI). Current femtoscopic studies are able to extract the size, shape, and orientation of the pair emission regions, as well as offer estimates of the total time to reach kinetic decoupling and the duration of particle emission [1, 2]. The momentum and species dependence of femtoscopic measurements affirm the collective nature of the hot and dense matter created in heavy-ion collisions [3–6]. Non-identical particle analyses additionally allow for the measurement of the space–time separation of the single particle source regions [5, 7–9].

In addition to characterizing the source region, femtoscopy allows one to extract nuclear scattering parameters, many of which are difficult or impossible to measure otherwise.  $\Lambda$ K pairs, which only interact strong, are the subject of this analysis. Calculations within Quantum Chromodynamics (QCD), the theory of the strong interaction, are notoriously difficult except in the regime of weak coupling, where perturbative methods may be applied. The  $\Lambda$ K analysis presented offers low energy QCD measurements, which fall into the non-perturbative regime of QCD. Therefore, the  $\Lambda$ K analysis not only gives insight into the strong interaction, it will also help guide future QCD calculations. Furthermore, the  $\Lambda$ K scattering parameters were not previously known, and theoretical predictions are limited. The extracted scattering parameters are compared to predictions obtained in the framework of chiral perturbation theory [10, 11]. Information about scattering parameters for similar systems are also very limited; past studies of kaon-proton scattering revealed the strong force is attractive in the  $K^-p$  interaction, and repulsive in that of the  $K^+p$  [12–14].

This paper presents the first measurements of the scattering parameters of  $\Lambda$ K pairs in all three charge combinations ( $\Lambda K^+$ ,  $\Lambda K^-$ , and  $\Lambda K_S^0$ ). The scattering parameters, along with pair emission source sizes, are extracted with a femtoscopic analysis of  $\Lambda$ K correlations in Pb–Pb collisions at  $\sqrt{s_{NN}} = 2.76$  TeV measured by the ALICE experiment at the LHC. These correlations result from strong final-state interactions, and are fit with a parametrization by Lednický and Lyuboshitz [15]. Extensive studies with the THERMINATOR 2 event generator are performed to account for both non-femtoscopic backgrounds as well as contributions from residual correlations induced by feed-down from particle decays.

The organization of this paper is as follows. In Sec. 2 the data selection methods are briefly discussed. In Sec. 3 the analysis techniques utilized in this study are presented. Here, the two-particle correlation function is introduced, as well as the theoretical models with which the data are fit. This section also includes descriptions of the handling of residual correlations, corrections accounting for finite track momentum resolution, treatment of the non-femtoscopic background, as well as a brief description of the systematic uncertainties estimation. The final results are presented in Sec. 4 and concluding remarks are given in Sec. 5. Appendix A demonstrates an alternate approach to forming correlation functions, whose purpose here is to help eliminate the non-femtoscopic background. Appendix B discusses the procedure needed to generate fit functions when both the strong and Coulomb interactions are present. In Appendix C, the THERMINATOR 2 event generator is used to demonstrate the effect on a one-dimensional femtoscopic fit of a non-zero space-time separation between the single particle sources. Throughout the text, the pair name is used as shorthand for the pair-conjugate system, which are found to be consistent (e.g.,  $\Lambda K^+$  for  $\Lambda K^+ \oplus \bar{\Lambda} K^-$ ,  $\Lambda K^-$  for  $\Lambda K^- \oplus \bar{\Lambda} K^+$ , and  $\Lambda K_S^0$  for  $\Lambda K_S^0 \oplus \bar{\Lambda} K_S^0$ ), and  $\Lambda$ K is used to describe all  $\Lambda$ K combinations.

## 2 Data analysis

This work reports on the analysis of Pb–Pb collisions at  $\sqrt{s_{NN}} = 2.76$  TeV produced by the LHC and measured by the ALICE experiment [16] in 2011. Approximately 40 million events were analyzed, which were classified according to their centrality percentiles determined using the measured amplitudes in the V0 detectors [17]. In order for an event to be included in the analysis, the position of the reconstructed event vertex must be within 10 cm of the center of the ALICE detector along the beam axis.

Charged particle tracking was performed using the Time Projection Chamber (TPC) [18] and the Inner Tracking System (ITS) [19]. The ITS allows for high spatial resolution of the primary (collision) vertex. The momenta were determined by the tracking algorithm using tracks reconstructed with the TPC only and constrained to the primary vertex. Tracks were selected from the central pseudorapidity region,  $|\eta| < 0.8$ . A minimum requirement of 80 reconstructed TPC clusters was imposed, the purpose of which is to ensure both the quality of the track and good transverse momentum ( $p_T$ ) resolution at large momenta, as well as to reject fake tracks.

Particle identification (PID) for reconstructed tracks was carried out using both the TPC and Time-Of-Flight (TOF) detectors [20, 21]. For TPC PID, a parametrized Bethe-Bloch formula was used to calculate the specific energy loss  $\langle dE/dx \rangle$  in the detector expected for a particle with a given mass and momentum. For TOF PID, the particle mass was used to calculate the expected time of flight as a function of track length and momentum. For each PID method, a value ( $N_\sigma$ ) was assigned to each track denoting the number of standard deviations between the measured track information and calculated values. This procedure was applied for four particle species hypotheses—electron, pion, kaon, and proton—and for each hypothesis a different  $N_\sigma$  value was obtained per detector.

### 2.1 $K^\pm$ selection

The single-particle selection criteria used to select charged kaon candidates are summarized in Table 1. Track reconstruction for the charged kaons was performed using the TPC, and tracks within the range  $0.14 < p_T < 1.5$  GeV/c were accepted for analysis. To reduce the number of secondary particles (e.g., charged particles produced in the detector material, particles from weak decays, etc.) in the sample, a selection criterion is established based on the maximum distance-of-closest-approach (DCA) of the track to the primary vertex. This is realized by imposing a restriction on the DCA in both the transverse and beam directions.

Particle identification was performed using both the TPC and TOF detectors via the  $N_\sigma$  method. The  $N_\sigma$  selection criteria become tighter with increasing momentum to reduce contamination within the samples, as the  $K^\pm$  signals begin to overlap more significantly with those from other particles, particularly  $e^\pm$  and  $\pi^\pm$ . Rejection procedures are included to reduce the contamination in the  $K^\pm$  samples from electrons and pions. The specifics for the  $K^\pm$  selection are contained in Table 1. The purity of the  $K^\pm$  collections,  $P_{K^\pm}$ , was estimated to be approximately 97% from a Monte-Carlo (MC) study based on HIJING [22] simulations using GEANT3 [23] to model particle transport through the ALICE detectors. For a more detailed estimate of the  $K^\pm$  purity from an analysis employing similar methods, see [24].

### 2.2 $K_S^0$ and $\Lambda$ selection

Electrically neutral  $\Lambda$  ( $\bar{\Lambda}$ ) and  $K_S^0$  particles are reconstructed through their weak decays:  $\Lambda \rightarrow p\pi^-$  ( $\bar{\Lambda} \rightarrow \pi^+\bar{p}$ ) and  $K_S^0 \rightarrow \pi^+\pi^-$ , with branching ratios 63.9% and 69.2% [25], respectively. The obtained candidates are denominated as  $V^0$  particles due to their decay topology. The selection criteria used are shown in Tables 2 and 3. Aside from kinematic and PID selection methods (using TPC and TOF detectors), the tracks of the decay products (called *daughters*) must also meet a minimum requirement on their impact parameter with respect to the primary vertex. The decay vertex of the  $V^0$  is calculated based on the positions in which the two daughter tracks were closest. To help in reducing combinatorial

**Table 1:** Selection criteria for  $K^\pm$  mesons

K <sup>±</sup> selection		
Transverse momentum $p_T$		$0.14 < p_T < 1.5 \text{ GeV}/c$
$ \eta $		$< 0.8$
Transverse DCA to primary vertex		$< 2.4 \text{ cm}$
Longitudinal DCA to primary vertex		$< 3.0 \text{ cm}$
TPC and TOF $N_\sigma$		
$p < 0.4 \text{ GeV}/c$		$N_{\sigma K, \text{TPC}} < 2$
$0.4 \leq p < 0.45 \text{ GeV}/c$		$N_{\sigma K, \text{TPC}} < 1$
$0.45 \leq p < 0.80 \text{ GeV}/c$		$N_{\sigma K, \text{TPC}} < 3$ $N_{\sigma K, \text{TOF}} < 2$
$0.80 \leq p < 1.0 \text{ GeV}/c$		$N_{\sigma K, \text{TPC}} < 3$ $N_{\sigma K, \text{TOF}} < 1.5$
$p \geq 1.0 \text{ GeV}/c$		$N_{\sigma K, \text{TPC}} < 3$ $N_{\sigma K, \text{TOF}} < 1$
Electron rejection: reject if all satisfied		$N_{\sigma e, \text{TPC}} < 3$ $N_{\sigma e, \text{TPC}} < N_{\sigma K, \text{TPC}}$ $N_{\sigma e, \text{TOF}} < N_{\sigma K, \text{TOF}}$
Pion rejection: reject if:		
$p < 0.65 \text{ GeV}/c$		TOF and TPC available
		$p < 0.5 \text{ GeV}/c$
		$0.5 \leq p < 0.65 \text{ GeV}/c$
$0.65 \leq p < 1.5 \text{ GeV}/c$		$N_{\sigma \pi, \text{TPC}} < 5$ $N_{\sigma \pi, \text{TOF}} < 3$
$p \geq 1.5 \text{ GeV}/c$		$N_{\sigma \pi, \text{TPC}} < 5$ $N_{\sigma \pi, \text{TOF}} < 2$

background, a maximum value is demanded on the distance of closest approach between the daughters (DCA  $V^0$  daughters). The positive and negative daughter tracks are combined to form the  $V^0$  candidate, the momentum of which is the sum of the momenta of the daughters calculated in the condition in which they were closest to one another.

To select primary candidates, the impact parameter with respect to the primary vertex is used as a selection criterion for each  $V^0$ . Furthermore, a restriction is imposed on the pointing angle,  $\theta_{PA}$ , between the  $V^0$  momentum and the vector pointing from the primary vertex to the secondary  $V^0$  decay vertex, which is achieved by appointing a minimum value on  $\cos(\theta_{PA})$  (“Cosine of pointing angle” in Tables 2 and 3).

In order to remove the contamination to the  $\Lambda$  ( $\bar{\Lambda}$ ) and  $K_S^0$  samples due to misidentification of the protons and pions for each  $V^0$ , the mass assuming different identities ( $\Lambda$ ,  $\bar{\Lambda}$ , and  $K_S^0$  hypotheses) is calculated and utilized in a misidentification procedure. The  $K_S^0$  hypothesis ( $m_{inv, K_S^0 \text{ hyp.}}$ ) is calculated assuming  $\pi^+\pi^-$  daughters, the  $\Lambda$  hypothesis ( $m_{inv, \Lambda \text{ hyp.}}$ ) assumes  $p\pi^-$  daughters, and the  $\bar{\Lambda}$  hypothesis ( $m_{inv, \bar{\Lambda} \text{ hyp.}}$ ) assumes  $\bar{p}\pi^+$  daughters. In the misidentification methods, the calculated masses are compared to the corresponding particle masses of the  $K_S^0$  and  $\Lambda$  ( $\bar{\Lambda}$ ),  $m_{PDG, K_S^0}$  and  $m_{PDG, \Lambda(\bar{\Lambda})}$  respectively, as recorded by the Particle Data Group [25]. For  $\Lambda$  ( $\bar{\Lambda}$ ) selection, a candidate is concluded to be misidentified and is rejected if all of the following criteria are satisfied:

1.  $|m_{inv, K_S^0 \text{ hyp.}} - m_{PDG, K_S^0}| < 9.0 \text{ MeV}/c^2$ ,
2. daughter particles pass daughter selection criteria intended for  $K_S^0$  reconstruction,
3.  $|m_{inv, K_S^0 \text{ hyp.}} - m_{PDG, K_S^0}| < |m_{inv, \Lambda(\bar{\Lambda}) \text{ hyp.}} - m_{PDG, \Lambda(\bar{\Lambda})}|$ .

Similarly, for  $K_S^0$  selection, a candidate is rejected if all of the following criteria are satisfied for the  $\Lambda$  case, or for the  $\bar{\Lambda}$  case:

1.  $|m_{inv, \Lambda(\bar{\Lambda}) \text{ hyp.}} - m_{PDG, \Lambda(\bar{\Lambda})}| < 9.0 \text{ MeV}/c^2$ ,
2. daughter particles pass daughter selection criteria intended for  $\Lambda$  ( $\bar{\Lambda}$ ) reconstruction,
3.  $|m_{inv, \Lambda(\bar{\Lambda}) \text{ hyp.}} - m_{PDG, \Lambda(\bar{\Lambda})}| < |m_{inv, K_S^0 \text{ hyp.}} - m_{PDG, K_S^0}|$ .

A final restriction on the invariant mass ( $m_{inv}$ ) is applied to enhance the purity. These selection criteria are shown in Tables 2 and 3. To avoid any auto-correlation effects, all  $V^0$  candidates within each single-particle collection ( $\Lambda$ ,  $\bar{\Lambda}$ , and  $K_S^0$  separately) are ensured to have unique daughters. If a daughter is found to be shared among  $V^0$  candidates in a given collection, only that with the smallest DCA to the primary vertex is kept. This procedure ensures unique single-particle collections before particle pairs are constructed; the elimination of shared daughters between the particles within each pair is described below in Sec. 2.3. The resulting invariant mass distributions for  $\Lambda$  and  $K_S^0$  collections in the 0–10% centrality interval are shown in Fig. 1. For the purity estimations, the background signal is extracted by fitting the  $m_{inv}$  distribution with a 4<sup>th</sup>-order polynomial outside of the mass peak and assuming the distribution to continue smoothly beneath the mass peak. The  $\Lambda$  and  $\bar{\Lambda}$  purities are estimated to be  $P_{\Lambda(\bar{\Lambda})} \approx 95\%$ , and that of the  $K_S^0$  is  $P_{K_S^0} \approx 98\%$ .

### 2.3 Pair construction

In order to reduce the contamination to the two-particle correlations due to pairs sharing daughters, track splitting (two tracks reconstructed from one particle), and track merging (one track reconstructed from

**Table 2:** Selection criteria for  $\Lambda$  and  $\bar{\Lambda}$  hyperons

$\Lambda$ selection	
Transverse momentum $p_T$	$> 0.4 \text{ GeV}/c$
$ \eta $	$< 0.8$
Invariant mass	$ m_{p\pi} - m_{\text{PDG}}  < 3.8 \text{ MeV}/c^2$
DCA to primary vertex	$< 0.5 \text{ cm}$
Cosine of pointing angle	$> 0.9993$
Decay length	$< 60 \text{ cm}$
$\pi$ and p daughter criteria	
$ \eta $	$< 0.8$
DCA $\pi$ p daughters	$< 0.4 \text{ cm}$
$\pi$ -specific	
$p_T$	$> 0.16 \text{ GeV}/c$
DCA to primary vertex	$> 0.3 \text{ cm}$
TPC and TOF $N_\sigma$	
$p < 0.5 \text{ GeV}/c$	$N_{\sigma,\text{TPC}} < 3$
$p \geq 0.5 \text{ GeV}/c$	TOF & TPC available $N_{\sigma,\text{TPC}} < 3$
	$N_{\sigma,\text{TOF}} < 3$
	Only TPC available $N_{\sigma,\text{TPC}} < 3$
p-specific	
$p_T$	$> 0.5(\text{p}) [0.3(\bar{\text{p}})] \text{ GeV}/c$
DCA to primary vertex	$> 0.1 \text{ cm}$
TPC and TOF $N_\sigma$	
$p < 0.8 \text{ GeV}/c$	$N_{\sigma,\text{TPC}} < 3$
$p \geq 0.8 \text{ GeV}/c$	TOF & TPC available $N_{\sigma,\text{TPC}} < 3$
	$N_{\sigma,\text{TOF}} < 3$
	Only TPC available $N_{\sigma,\text{TPC}} < 3$

**Table 3:** Selection criteria for  $K_S^0$  mesons

$K_S^0$ selection	
Transverse momentum $p_T$	$> 0.2 \text{ GeV}/c$
$ \eta $	$< 0.8$
Invariant mass	$0.480 < m_{\pi^+\pi^-} < 0.515 \text{ GeV}/c^2$
DCA to primary vertex	$< 0.3 \text{ cm}$
Cosine of pointing angle	$> 0.9993$
Decay length	$< 30 \text{ cm}$
$\pi^\pm$ daughter criteria	
$p_T$	$> 0.15 \text{ GeV}/c$
$ \eta $	$< 0.8$
DCA $\pi^+\pi^-$ daughters	$< 0.3 \text{ cm}$
DCA to primary vertex	$> 0.3 \text{ cm}$
TPC and TOF $N_\sigma$	
$p < 0.5 \text{ GeV}/c$	$N_{\sigma,\text{TPC}} < 3$
$p \geq 0.5 \text{ GeV}/c$	TOF & TPC available $N_{\sigma,\text{TPC}} < 3$
	$N_{\sigma,\text{TOF}} < 3$
	Only TPC available $N_{\sigma,\text{TPC}} < 3$

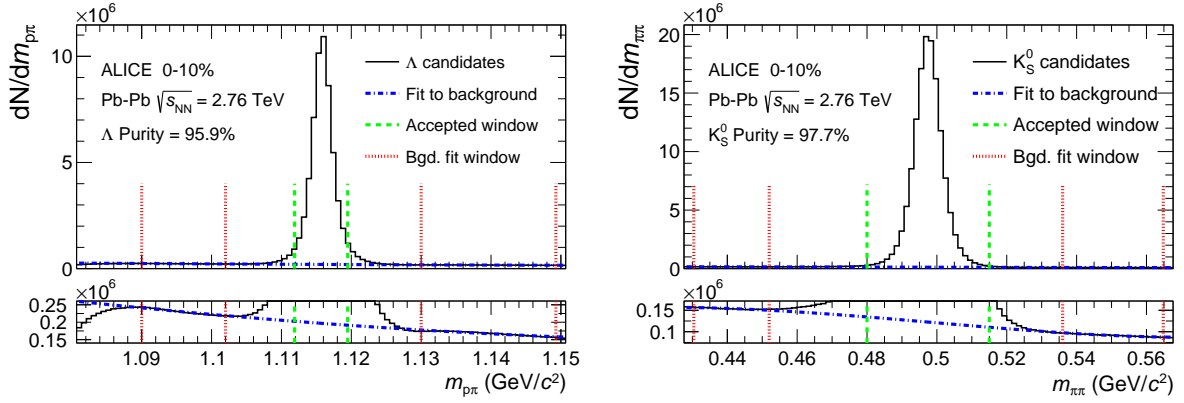


**Figure 1:** (Color online) Invariant mass distributions in the 0–10% centrality interval of (a)  $p\pi^+$  pairs showing the  $\Lambda$  peak, and of (b)  $\pi^+\pi^-$  pairs showing the  $K_S^0$  peak, for  $V^0$  candidates. The bottom panels are zoomed to show the background with fit. The vertical dashed (green) lines represent the selection restrictions used in the analyses, the vertical dotted (red) lines delineate the region over which the background was fit, and the dash-dotted (blue) line shows the background fit.

two particles), two main pair rejection procedures are applied: a shared daughter restriction, and an average separation constraint. The purpose of the shared daughter restriction is to ensure the first particle in the pair is unique from the second. For pairs formed of two  $V^0$ s (i.e.,  $\Lambda K_S^0$ ), this is implemented by removing all pairs which share a daughter. For a pair formed of a single  $V^0$  and a charged track (i.e.,  $\Lambda K^\pm$ ), the restriction removes all pairs in which the charged track is also claimed as a daughter of the  $V^0$ .

The purpose of the average separation constraint is to remove splitting and merging effects, and it is employed in the following way. The average separation between two tracks is calculated using their spatial separation as determined at several points throughout the TPC (every 20 cm radially from 85 cm to 245 cm). For the  $\Lambda K_S^0$  analysis, which involves two  $V^0$  particles, a minimum average separation constraint of 6 cm between the like-charge daughters in the pairs is imposed (for example, between the p daughter of the  $\Lambda$  and the  $\pi^+$  daughter of the  $K_S^0$ ). For the  $\Lambda K^\pm$  analyses, a minimum average separation constraint of 8 cm is enforced between the  $K^\pm$  and the  $\Lambda$  daughter sharing the same charge (for example, in the  $\Lambda K^+$  analysis, between the p daughter of the  $\Lambda$  and the  $K^+$ ). Splitting and merging effects between oppositely charged tracks were found to be negligible, therefore no constraints on unlike-charge tracks are imposed.

### 3 Analysis methods

#### 3.1 Correlation function

The two-particle correlation function for particles  $a$  and  $b$ ,  $C_{ab}(\vec{p}_a, \vec{p}_b)$ , is defined as the ratio of the probability of simultaneously measuring two particles with momenta  $p_a$  and  $p_b$ , to the product of the single-particle probabilities. These probabilities are directly related to the covariant two-particle spectrum,  $E_a E_b \frac{d^6 N_{ab}}{d^3 p_a d^3 p_b}$ , and the single-particle spectra,  $E_{a(b)} \frac{d^3 N_{a(b)}}{d^3 p_{a(b)}}$ , and the correlation function may be written

$$C_{ab}(\vec{p}_a, \vec{p}_b) = \frac{E_a E_b \frac{d^6 N_{ab}}{d^3 p_a d^3 p_b}}{\left(E_a \frac{d^3 N_a}{d^3 p_a}\right) \left(E_b \frac{d^3 N_b}{d^3 p_b}\right)}, \quad (1)$$

where  $N_{ab}$  is the yield of particle pairs,  $E_{a(b)}$  is the energy,  $p_{a(b)}$  is the three-momentum, and  $N_{a(b)}$  is the yield of particles  $a(b)$ . Theoretically, the correlation function may be expressed as in the Koonin-Pratt

equation [26, 27],

$$C(\mathbf{k}^*) = \int S_{\mathbf{P}}(\mathbf{r}^*) |\Psi_{\mathbf{k}^*}(\mathbf{r}^*)|^2 d^3\mathbf{r}^*, \quad (2)$$

where  $\mathbf{k}^*$  is the relative momentum of the pair (defined as  $\mathbf{k}^* = \frac{1}{2}|\mathbf{p}_1^* - \mathbf{p}_2^*|$ , where  $\mathbf{p}_1^*$  and  $\mathbf{p}_2^*$  are the momenta of the two particles) in the pair rest frame (PRF),  $\mathbf{r}^*$  is the relative separation in the same frame,  $\mathbf{P}$  is the total pair momentum,  $S_{\mathbf{P}}(\mathbf{r}^*)$  is the pair source distribution, and  $\Psi_{\mathbf{k}^*}(\mathbf{r}^*)$  is the two-particle wave-function.

In practice, the correlation function is formed experimentally as

$$C(k^*) = \mathcal{N} \frac{A(k^*)}{B(k^*)}, \quad (3)$$

where  $A(k^*)$  is the signal distribution,  $B(k^*)$  is the reference distribution, and  $\mathcal{N}$  is a normalization parameter. The reference distribution is used to divide out the phase-space effects, leaving only the physical effects in the correlation function. The normalization parameter is chosen such that the mean value of the correlation function equals unity for  $k^* \in [0.32, 0.4]$  GeV/c. The signal distribution is the same-event distribution of particle pairs. The reference distribution,  $B(k^*)$ , is obtained using mixed-event pairs [28], i.e., particles from a given event are paired with those from another event. Other techniques exist; most notably, one may use same-event pairs after rotating one particle in the pair by  $180^\circ$  in the transverse plane (see Sec. 3.5 and App. A for more details). For this analysis, each event is mixed with five others for the reference distribution construction. To be included in the mixing pool, an event must contain at least one particle of each type from the pair of interest (e.g., for the  $\Lambda K_S^0$  analysis, an accepted event must contain at least one  $\Lambda$  and at least one  $K_S^0$ ). In order to mix similar events, only those of like centrality (within 5%) and of like primary vertex position (within 2 cm) are combined.

This analysis presents correlation functions for three centrality percentile ranges (0–10%, 10–30%, and 30–50%), and is integrated in pair transverse momentum ( $k_T = \frac{1}{2}|\mathbf{p}_{T,1} + \mathbf{p}_{T,2}|$ ) due to limited data. The  $k_T$  dependences of the three  $\Lambda K$  charge combinations should be comparable, so an integrated analysis is acceptable.

### 3.2 Modeling the correlation function

In the absence of the Coulomb interaction, the correlation function can be described analytically with a model derived by Lednický and Lyuboshitz [15]. Within the model, the (non-symmetrized) two-particle wave function is expressed as a superposition of a plane wave and diverging spherical wave, and the complex scattering amplitude,  $f^S(k^*)$ , is evaluated via the effective range approximation,

$$f^S(k^*) = \left( \frac{1}{f_0^S} + \frac{1}{2}d_0^S k^{*2} - ik^* \right)^{-1}, \quad (4)$$

where  $f_0^S$  is the complex s-wave scattering length,  $d_0^S$  is the effective range of the interaction, and  $S$  denotes the total spin of the particular pair. The sign convention is such that a positive real component of the scattering length,  $\Re f_0$ , represents an attractive interaction, while a negative value represents a repulsion. A spherically symmetric Gaussian distribution with radius  $R_{\text{inv}}$  is assumed for the pair emission source in the PRF. With these assumptions, utilizing the Koonin-Pratt equation (Eq. (2)), the correlation function for non-identical particle pairs is modeled by [15]

$$C(k^*)_{\text{Lednický}} = 1 + \sum_S \rho_S \left[ \frac{1}{2} \left| \frac{f^S(k^*)}{R_{\text{inv}}} \right|^2 \left( 1 - \frac{d_0^S}{2\sqrt{\pi}R_{\text{inv}}} \right) + \frac{2\Re f^S(k^*)}{\sqrt{\pi}R_{\text{inv}}} F_1(2k^*R_{\text{inv}}) - \frac{\Im f^S(k^*)}{R_{\text{inv}}} F_2(2k^*R_{\text{inv}}) \right], \quad (5)$$



where  $\Re f^S(k^*)$  and  $\Im f^S(k^*)$  denote the real and imaginary parts of the complex scattering length, respectively, and  $F_1$  and  $F_2$  are analytic functions [15]. The weight factor,  $\rho_S$ , is the normalized emission probability for a state of total spin  $S$ ; in the assumed case of unpolarized emission,  $\rho_S = (2S+1)/[(2j_1+1)(2j_2+1)]$ , where  $j_{1,2}$  are the spins of the particles in the pair. The  $\Lambda$  hyperon is spin-1/2 and K mesons are spin-0, so the  $\Lambda K$  system only has one possible total spin state  $S$ , and therefore  $C(k^*)$  in Eq. (5) has only a single term. In the following, the  $S$  superscript is dropped from all scattering parameters.

### 3.3 Residual correlations

The purpose of this analysis is to study the interaction and scale of the emitting source of the primary  $\Lambda K$  pairs. However, in practice some of the selected particles originate as products from other decaying particles, and some of the final pairs contain a misidentified member. In both cases, these contribute to the observed correlation function, and obscure its relation to the primary  $\Lambda K$  system. The net contribution from fake pairs, which contain at least one misidentified member, is taken to average to unity, in which case they simply attenuate the femtoscopic signal. Pairs in which at least one member originates from a particle decay (e.g.,  $\Lambda K^+$  from  $\Sigma^0 K^+$ ) carry information about the parent system. In effect, the correlation between the parents will be visible, although smeared out, in the daughters' signal. This is termed a residual correlation resulting from feed-down. As described in the following, the main sources of residual correlations in the  $\Lambda K$  systems result from  $\Lambda$  hyperons which have decayed from  $\Sigma^0$ ,  $\Xi^0$ , and  $\Xi^-$  parents.

The measured correlation function is a combination of the genuine  $\Lambda K$  correlation with contributions from particle decays and impurities [29],

$$C_{\text{measured}}(k_{\Lambda K}^*) = 1 + \sum_{ij} \lambda'_{ij} [C_{ij}(k_{\Lambda K}^*) - 1], \quad (6)$$

with

$$\begin{aligned} \lambda'_{ij} &= \lambda_{\text{Fit}} \lambda_{ij}, \\ \sum_{ij} \lambda'_{ij} &= \lambda_{\text{Fit}} \sum_{ij} \lambda_{ij} = \lambda_{\text{Fit}}, \end{aligned} \quad (7)$$

where the  $ij$  terms include the primary  $\Lambda K$  contribution together with the contributions from residual feed-down and impurities. More specifically,  $C_{ij}(k_{\Lambda K}^*)$  is the correlation function of the parent system expressed in terms of the relative momentum of the daughter  $\Lambda K$  pair. The  $\lambda_{ij}$  parameters serve as weights dictating the relative strength of each component's contribution to the observed signal, and are normalized to unity (i.e.,  $\sum_{ij} \lambda_{ij} = 1$ , where  $ij$  includes also the primary  $\Lambda K$  component) [29, 30]. When the experimental correlation functions are fit, the individual  $\lambda_{ij}$  are fixed (and whose values can be found in Table 4), but the parameter  $\lambda_{\text{Fit}}$  in Eq. (6) is left free.

To model the parent correlation function expressed in the relative momentum of the daughter pair, a transform matrix is utilized,

$$C_{ij}(k_{\Lambda K}^*) \equiv \frac{\sum_{k_{ij}^*} C_{ij}(k_{ij}^*) T(k_{ij}^*, k_{\Lambda K}^*)}{\sum_{k_{ij}^*} T(k_{ij}^*, k_{\Lambda K}^*)}, \quad (8)$$

where  $T(k_{ij}^*, k_{\Lambda K}^*)$  is the transform matrix, which is generated with the THERMINATOR 2 [31] simulation. The transform matrix describes the decay kinematics of the parent system into the daughter system, and is essentially an unnormalized probability distribution mapping the  $k^*$  of the parent pair to that of the daughter pair when one or both parents decay (see [29] for more details).

The contribution of a parent system (e.g.,  $\Sigma^0 K^+$ ) to the daughter correlation function (e.g.,  $\Lambda K^+$ ) in the fit procedure is determined by modeling the parent system's correlation function and running it through the appropriate transform matrix. Since the interactions between these particles are not known, some

assumptions must be made. When modeling the parent systems, the source radii are assumed to be equal to those of the daughter  $\Lambda$ K systems. Furthermore, Coulomb-neutral parent pairs are assumed to share the same scattering parameters as the  $\Lambda$ K daughter pair, and the parent correlation function is modeled using Eq. (5). During the fit process, these source radii and scattering parameters are left free, as described in Sec. 3.6. For the  $\Xi^-K^\pm$  parent system, where the constituents interact via both the strong and Coulomb interactions, no analytical expression exists to model the correlation function (see App. B), and the experimental  $\Xi^-K^\pm$  data are used. However, the  $\Xi^-K^\pm$  correlation function is dominated by the contribution from the Coulomb interaction, and may be sufficiently modeled with a Coulomb-only scenario (in which the strong interaction is assumed to be negligible) for this analysis, to yield consistent results.

The  $\lambda_{ij}$  parameters dictate the relative strength of each contribution to the correlation function, and can be estimated using the THERMINATOR 2 and HIJING simulations. More specifically, a  $\lambda_{ij}$  parameter is estimated as the total number of  $\Lambda$ K pairs in the sample originating from source  $ij$  ( $N_{ij}$ ) divided by the total number of  $\Lambda$ K pairs. For a given  $\Lambda$ K source, the number of detected pairs depends on both the raw yield and the reconstruction efficiency. The relevant reconstruction efficiencies are those of the daughters under study, not of the parent particles; e.g., when determining the contribution of the  $\Xi^-K^+$  system to the  $\Lambda K^+$  correlation function, the reconstruction efficiency of the  $\Xi^-$  is not relevant, but that of the secondary  $\Lambda$  originating from a  $\Xi^-$  decay is. The reconstruction efficiencies ( $RE_{ij}$ ) are estimated with HIJING simulations using GEANT3 to model particle transport through the detector. HIJING events are generated from a superposition of PYTHIA pp collisions, and lack the strangeness saturation of a fully thermalized medium. As a result, HIJING is unreliable in providing the yields needed for this analysis, and, instead, the yields are estimated with the THERMINATOR 2 simulation ( $N_{ij}^{THERM}$ ). The number of  $\Lambda$ K pairs from source  $ij$  is then estimated as the product of the yield with the associated reconstruction efficiency,  $N_{ij} = N_{ij}^{THERM} RE_{ij}^{HIJING}$ . Finally, the  $\lambda_{ij}$  are estimated as

$$\lambda_{ij} = \frac{N_{ij}}{N_{Total}} = \frac{N_{ij}^{THERM} RE_{ij}^{HIJING}}{\sum_{\alpha\beta} N_{\alpha\beta}^{THERM} RE_{\alpha\beta}^{HIJING}}. \quad (9)$$

Femtoscopic analyses are sensitive to the pair emission structure at kinetic freeze-out. Therefore, within femtoscopy, any particle which originates from a particle decay before last rescattering is considered primary. The THERMINATOR 2 simulation shows that the  $\Lambda$  hyperons and K mesons decay from a large number of particle species ( $\sim 50$   $\Lambda$  parent species, and  $\sim 70$  K parent species), and the most significant contributing pair systems are  $\Sigma^0 K$ ,  $\Xi^- K$ ,  $\Xi^0 K$ ,  $\Sigma^{*+} K$ ,  $\Sigma^{*-} K$ ,  $\Sigma^{*0} K$ ,  $\Lambda K^*$ ,  $\Sigma^0 K^*$ ,  $\Xi^- K^*$ , and  $\Xi^0 K^*$ . However, the simulation does not include a hadronic rescattering phase, and not all of the aforementioned pair systems will survive until kinetic freeze-out. The systems resulting from electromagnetic or weak decays ( $\Sigma^0$ ,  $\Xi^-$ , and  $\Xi^0$ ) will survive long after kinetic freeze-out, and will contribute residual signals to the  $\Lambda$ K correlation functions. The majority of the remaining contributors decay via the strong interaction with mean proper lifetimes less than a few fm/c, and whose daughters should always be considered primary. The mean proper lifetime of the parent is used to judge whether or not the daughter is treated as primary. A decay product is considered primary if its parent has a mean proper lifetime  $\tau$  satisfying  $\tau < \tau_{max}$ , where  $c\tau_{max} = 10$  fm for this analysis. Changing  $\tau_{max}$  only moderately affects the  $\lambda_{ij}$  parameters, and the effect is included in the estimation of the systematic uncertainties. In order for a pair to be considered primary, both particles in the pair must be considered primary. If either parent has  $\tau > \tau_{max}$ , the daughter pair contributes to the “Other” category when calculating  $\lambda_{ij}$  parameters. For this mixture of pair systems, all with different two-particle interactions and single-particle source distributions, the net correlation effect is taken to average to unity.

Residual contributions from  $\Sigma^0$ ,  $\Xi^0$ ,  $\Xi^-$  are accounted for in the fit. The  $\lambda_{ij}$  values used can be found in Table 4, which also includes values for “Other” and “Fakes”. The “Other” category contains pairs which are not considered primary, and which do not originate from the residual contributors accounted for in

the fit. The “Fakes” category represents pairs that are mistakenly identified as  $\Lambda K$ . To estimate the  $\lambda_{\text{Fakes}}$  value, the number of fake pairs is assumed to be equal to the total number of simulated pairs multiplied by  $(1 - PP_{\Lambda K})/PP_{\Lambda K}$ , where  $PP_{\Lambda K}$  is the  $\Lambda K$  pair purity, estimated as the product of the two single-particle purities ( $PP_{\Lambda K} = P_{\Lambda}P_K$ ). More simply, this amounts to  $\lambda_{\text{Fakes}} = 1 - PP_{\Lambda K}$ . The correlations in both of these categories (“Other” and “Fakes”) are assumed to average to unity, and pairs in these categories therefore only contribute by attenuating the signal.

**Table 4:** Weight parameters ( $\lambda_{ij}$ ) for the individual components of the  $\Lambda K$  correlation functions

$\Lambda K^+$		$\bar{\Lambda} K^-$		$\Lambda K^-$		$\bar{\Lambda} K^+$	
Source	$\lambda$ value	Source	$\lambda$ value	Source	$\lambda$ value	Source	$\lambda$ value
Primary	0.509	Primary	0.509	Primary	0.509	Primary	0.510
$\Sigma^0 K^+$	0.108	$\bar{\Sigma}^0 K^-$	0.107	$\Sigma^0 K^-$	0.107	$\bar{\Sigma}^0 K^+$	0.108
$\Xi^0 K^+$	0.037	$\bar{\Xi}^0 K^-$	0.034	$\Xi^0 K^-$	0.037	$\bar{\Xi}^0 K^+$	0.035
$\Xi^- K^+$	0.048	$\bar{\Xi}^+ K^-$	0.044	$\Xi^- K^-$	0.048	$\bar{\Xi}^+ K^+$	0.045
Other	0.218	Other	0.228	Other	0.221	Other	0.225
Fakes	0.079	Fakes	0.079	Fakes	0.079	Fakes	0.079

$\Lambda K_S^0$		$\bar{\Lambda} K_S^0$	
Source	$\lambda$ value	Source	$\lambda$ value
Primary	0.531	Primary	0.532
$\Sigma^0 K_S^0$	0.118	$\bar{\Sigma}^0 K_S^0$	0.118
$\Xi^0 K_S^0$	0.041	$\bar{\Xi}^0 K_S^0$	0.038
$\Xi^- K_S^0$	0.053	$\bar{\Xi}^+ K_S^0$	0.049
Other	0.189	Other	0.195
Fakes	0.069	Fakes	0.069

### 3.4 Momentum resolution corrections

Finite track momentum resolution causes the reconstructed relative momentum ( $k_{\text{Rec}}^*$ ) of a pair to differ from the true value ( $k_{\text{True}}^*$ ). This is accounted for through the use of a response matrix generated with HIJING simulations. With this approach, the resolution correction is applied on-the-fly during the fitting process by propagating the theoretical (fit) correlation function through the response matrix, according to

$$C(k_{\text{Rec}}^*) = \frac{\sum_{k_{\text{True}}^*} M_{k_{\text{Rec}}^*, k_{\text{True}}^*} C(k_{\text{True}}^*)}{\sum_{k_{\text{True}}^*} M_{k_{\text{Rec}}^*, k_{\text{True}}^*}}, \quad (10)$$

where  $M_{k_{\text{Rec}}^*, k_{\text{True}}^*}$  is the response matrix,  $C_{\text{fit}}(k_{\text{True}}^*)$  is the fit as a function of  $k_{\text{True}}^*$ , and the denominator normalizes the result.

### 3.5 Non-femtoscopic background

A significant non-femtoscopic background is observed in all of the studied  $\Lambda K$  correlations, which increases with decreasing centrality, is the same amongst all  $\Lambda K^{\pm}$  pairs, and is more pronounced in the  $\Lambda K_S^0$  system (the difference in  $\Lambda K^{\pm}$  and  $\Lambda K_S^0$  backgrounds is due mainly to a difference in kinematic selection criteria). The background is primarily due to particle collimation associated with elliptic flow, and results from mixing events with unlike event planes [32]. The effect produces the observed suppression at intermediate  $k^*$ , and should also lead to an enhancement at low  $k^*$ . To best describe the experimental

data, an understanding of the non-femtoscopic background is needed in the low  $k^*$  femtoscopic signal region, but an isolated view of it is only possible outside of such a region.

The THERMINATOR 2 simulation has been shown to reproduce the background features in a  $\pi K$  analysis [32]. Figure 2 shows the THERMINATOR 2 simulation together with experimental data. The figure also shows a 6<sup>th</sup>-order polynomial fit to the simulation, as well as the fit polynomial scaled to match the data. Clearly, the THERMINATOR 2 simulation offers a good description of the non-femtoscopic backgrounds in the  $\Lambda K$  systems, and can be used in a quantitative fashion to help fit the data. More specifically, the non-femtoscopic backgrounds are modeled by 6<sup>th</sup>-order polynomial fits to THERMINATOR 2 simulation,

$$F_{THERM.Bgd}(k^*) = ak^{*6} + bk^{*5} + ck^{*4} + dk^{*3} + ek^{*2} + fk^* + g, \quad (11)$$

where the linear term coefficient is fixed to zero ( $f = 0$ ), and one polynomial is fit for each centrality class and  $\Lambda K$  charge combination.

Before fitting the signal region of the experimental data, the coefficients of each polynomial are fixed by fits to the THERMINATOR 2 background, shown in Fig. 2. The extracted polynomial is adjusted to best describe the experimental data by introducing a scale factor and a vertical shift,

$$F_{Bgd}(k^*) = \alpha \cdot F_{THERM.Bgd}(k^*) + \beta, \quad (12)$$

where  $\alpha$  and  $\beta$  are determined by fitting to the data in the region  $0.32 < k^* < 0.80$  GeV/c; all of the background parameters in Eq. (11) and Eq. (12) are fixed before fitting the low- $k^*$  signal region of the experimental correlation functions. In all cases, the non-femtoscopic background correction was applied as a multiplicative factor to the correlation function during the fitting process.

An alternative approach to treating the non-femtoscopic background is to instead attempt to eliminate it. The background may be effectively reduced by forming the reference distribution ( $B(k^*)$ ) with the “Stavinskiy method”. With the Stavinskiy method, mixed-event pairs are not used for the reference distribution; instead, same-event pseudo-pairs, formed by rotating one particle in a real pair by 180° in the transverse plane, are used. This rotation rids the pairs of any femtoscopic correlation, while maintaining correlations due to elliptic flow (and other suitably symmetric contributors). The flattening effect of the method on the  $\Lambda K^+$  correlation functions can be seen in the appendix, in Fig. A.1.

### 3.6 Summarized correlation function construction

The parameters included in the generation of a model correlation function are:  $\lambda_{Fit}$ ,  $R$ ,  $f_0$  ( $\Re f_0$  and  $\Im f_0$  separately),  $d_0$ , and normalization  $\mathcal{N}$ . For the fit, a given pair and its conjugate (e.g.,  $\Lambda K^+$  and  $\bar{\Lambda} K^-$ ) share scattering parameters ( $\Re f_0$ ,  $\Im f_0$ ,  $d_0$ ), and the three distinct analyses ( $\Lambda K^+$ ,  $\Lambda K^-$ , and  $\Lambda K_S^0$ ) are assumed to have unique scattering parameters which are allowed to differ from each other. The pair emission source for a given centrality class is assumed similar among all analyses; therefore, for each centrality, all  $\Lambda K$  analyses share a common radius parameter,  $R$ . For each centrality class, a single  $\lambda_{Fit}$  parameter (see Eq. (6)) is shared amongst all. Each fit correlation function has a unique normalization parameter,  $\mathcal{N}$ . The experimental correlation functions were constructed separately for the two different field polarities applied by the ALICE L3 solenoid magnet during the data acquisition. These are kept separate during the fitting process, and are combined using a weighted average when plotting, where the weight is the number of numerator pairs in the normalization range.

All experimental correlation functions are normalized in the range  $0.32 < k^* < 0.40$  GeV/c, and fit in the range  $0.0 < k^* < 0.30$  GeV/c. For the  $\Lambda K^-$  analysis, the region  $0.19 < k^* < 0.23$  GeV/c was excluded from the fit to exclude the bump caused by the  $\Omega^-$  decay. For each pair system, contributions from three residual contributors are accounted for, as discussed in Sec. 3.3, whose individual  $\lambda$  values are listed in Table 4. Effects of finite track momentum resolution are also accounted for, as outlined in Sec. 3.4.

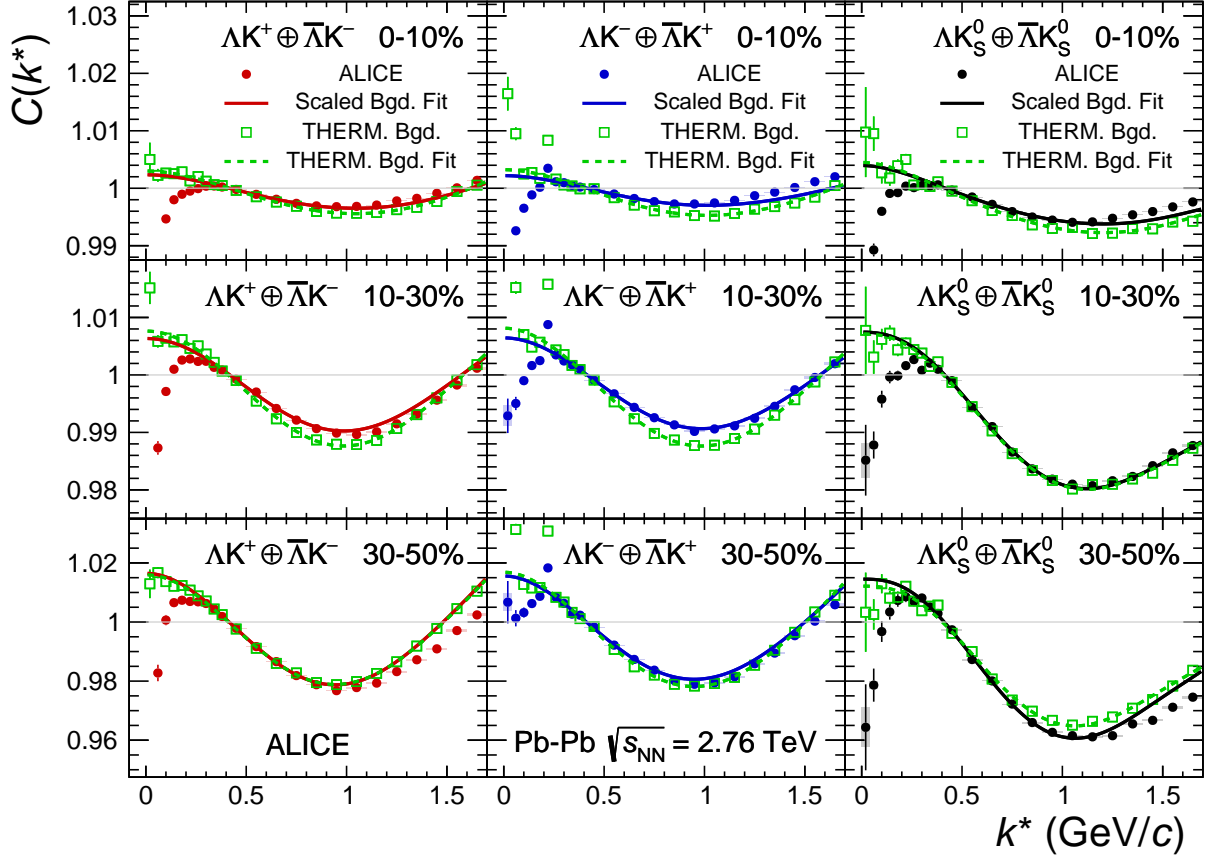


**Figure 2:** (Color online) THERMINATOR 2 simulation (open squares) together with experimental data (closed circles). Results are shown for  $\Lambda K^+$  (left),  $\Lambda K^-$  (middle), and  $\Lambda K_S^0$  (right). Rows differentiate the different centrality intervals (0–10% in the top, 10–30% in the middle, and 30–50% in the bottom). A 6<sup>th</sup>-order polynomial fit to the simulation is shown as a dashed curve. This polynomial is scaled to match the experimental data and is drawn as a solid curve.

The non-femtoscopic backgrounds are modeled using the THERMINATOR 2 simulation, as described in Sec. 3.5. A log-likelihood fit function is used as the statistic quantifying the quality of the fit [1].

The complete fit function is constructed as follows. The uncorrected, primary, fit correlation function,  $C_{\Lambda K}(k_{\Lambda K, \text{True}}^*)$ , is constructed using Eq. (5). The model correlation functions describing the parent systems which contribute via residual correlations,  $C_{ij}(k_{ij, \text{True}}^*)$ , are obtained using Eq. (5) for Coulomb-neutral pairs or experimental data for  $\Xi^- K^\pm$  contributions. The residual contributions are then found by running each parent correlation function through the appropriate transform matrix, via Eq. (8). The model primary and residual correlations are combined, via Eq. (6) with Tab. 4, to form  $C'_{\text{Fit}}(k_{\text{True}}^*)$ . Corrections are applied to account for momentum resolution effects using Eq. (10), to obtain  $C'_{\text{Fit}}(k_{\text{Rec}}^*)$ . Finally, the non-femtoscopic background correction,  $F_{\text{Bgd}}(k_{\text{Rec}}^*)$ , is applied and the final fit function is obtained,

$$C_{\text{Fit}}(k_{\text{Rec}}^*) = \mathcal{N} \cdot F_{\text{Bgd}}(k_{\text{Rec}}^*) \cdot C'_{\text{Fit}}(k_{\text{Rec}}^*), \quad (13)$$

where  $\mathcal{N}$  is a normalization parameter. This model correlation function is then fit to the experimental correlation function.

### 3.7 Systematic uncertainties

To estimate the systematic uncertainties in the analysis, the selection criteria were varied, and experimental correlation functions and fit results were obtained for each variation. To quantify the systematic

uncertainties on the data, the experimental correlation functions from each variation of the selection criteria were averaged, and the standard deviations were calculated for each data point. The systematic uncertainties of the correlation functions were set to these calculated standard deviations.

A similar process was followed for estimating the systematic uncertainties of the extracted fit parameters. Namely, the extracted fit parameters from each variation were averaged, and the resulting standard deviations taken as the systematic uncertainties. Additionally, a systematic analysis was done on the fit method through varying the  $k^*$  fit range, varying the modeling of the non-femtoscopic background, as well as varying  $\tau_{\max}$  in the treatment of residual correlations. The choice of  $k^*$  fit range was varied by  $\pm 25\%$ . In addition to modeling with a polynomial fit to the THERMINATOR 2 simulation, the backgrounds of all of the systems were modeled by fitting to the data with a linear, quadratic, and Gaussian form. Finally,  $\tau_{\max}$  was varied from the default value of  $\tau_{\max} = 10$  fm/c down to  $\tau_{\max} = 6$  fm/c and up to  $\tau_{\max} = 15$  fm/c. The resulting uncertainties in the extracted parameter sets were combined with the uncertainties arising from the variations of the selection criteria. The systematic uncertainties of the extracted parameters sets are due primarily to the fit method variations, i.e., the selection criteria do not contribute significantly.

## 4 Results

Figure 3 shows the  $\Lambda K$  data with fits for all studied centrality percentile intervals (0–10%, 10–30%, and 30–50%). All six  $\Lambda K$  systems ( $\Lambda K^+$ ,  $\bar{\Lambda} K^-$ ,  $\Lambda K^-$ ,  $\bar{\Lambda} K^+$ ,  $\Lambda K_S^0$ ,  $\bar{\Lambda} K_S^0$ ) are fit simultaneously across all centralities, with a single radius and normalization  $\lambda_{\text{Fit}}$  parameter for each centrality interval. The figure shows the primary ( $\Lambda K$ ) contribution to the fit (i.e.,  $1 + \lambda'_{\Lambda K} C_{\Lambda K}(k_{\Lambda K}^*)$  in Eq. (6)), the fit to the non-femtoscopic background, and the final fit, with all residual contributions included and after all corrections have been applied. The extraction of the primary  $\Lambda K$  component is the purpose of this study. The figure demonstrates that the final fit function is similar to the primary  $\Lambda K$  component, with the largest differences between the two observed in the 30–50% centrality interval due mainly to the large contribution of the non-femtoscopic background.

Figure 4 (left) summarizes the extracted  $\Lambda K$  scattering parameters, and includes theoretical predictions made using chiral perturbation theory [10, 11]. For all  $\Lambda K$  systems, positive imaginary parts of the scattering lengths,  $\Im(f_0)$ , are extracted from the experimental data. This is expected, as  $\Im(f_0)$  describes the inelastic scattering channels. More interestingly, the results show that the  $\Lambda K^+$  and  $\Lambda K^-$  systems differ in the sign of the real part,  $\Re(f_0)$ , of their scattering lengths, with a negative value for  $\Lambda K^+$  and positive value for  $\Lambda K^-$ . The  $\Re f_0$  extracted for the  $\Lambda K_S^0$  system is positive, and within uncertainties of that of  $\Lambda K^-$ . The real part of the scattering length describes the effect of the strong interaction: a positive  $\Re(f_0)$  signifies that the interaction is attractive, while a negative  $\Re(f_0)$  signifies a repulsive interaction, as is the usual convention in femtoscopy. Therefore, the femtoscopic signals from this analysis demonstrate that the strong interaction acts repulsively in the  $\Lambda K^+$  system, and acts attractively in the  $\Lambda K^-$  and  $\Lambda K_S^0$  systems. Finally, the results indicate that the effective range of the interaction,  $d_0$ , is positive in the  $\Lambda K^+$  system and negative in the  $\Lambda K^-$  and  $\Lambda K_S^0$  systems.

In Fig. 4 (left), the predictions of [10] do not distinguish the  $K\Lambda$  and  $K\bar{\Lambda}$  interactions and results are shown for two different parameter sets, whereas [11] offers unique  $K\Lambda$  and  $K\bar{\Lambda}$  scattering parameters for a single parameter set. In all cases, the predicted scattering parameters have both positive real and imaginary components, which is inconsistent with the  $\Lambda K^+$  system. Past studies of kaon-proton scattering found the  $K^-p$  interaction to be attractive, and that of the  $K^+p$  to be repulsive [12–14]. With respect to the kaons, this is similar to the current finding of an attractive  $\Lambda K^-$  interaction and a repulsive  $\Lambda K^+$  interaction. This difference could arise from different quark–antiquark interactions between the pairs ( $s\bar{s}$  in  $\Lambda K^+$ ,  $u\bar{u}$  in  $\Lambda K^-$ ). A related explanation could be that the effect is due to the different net strangeness for each system. The quark content of the  $\Lambda$  ( $\bar{\Lambda}$ ) is  $uds$  ( $\bar{u}\bar{d}\bar{s}$ ), that of the  $K^+$  ( $K^-$ ) is  $u\bar{s}$  ( $\bar{u}s$ ), and the

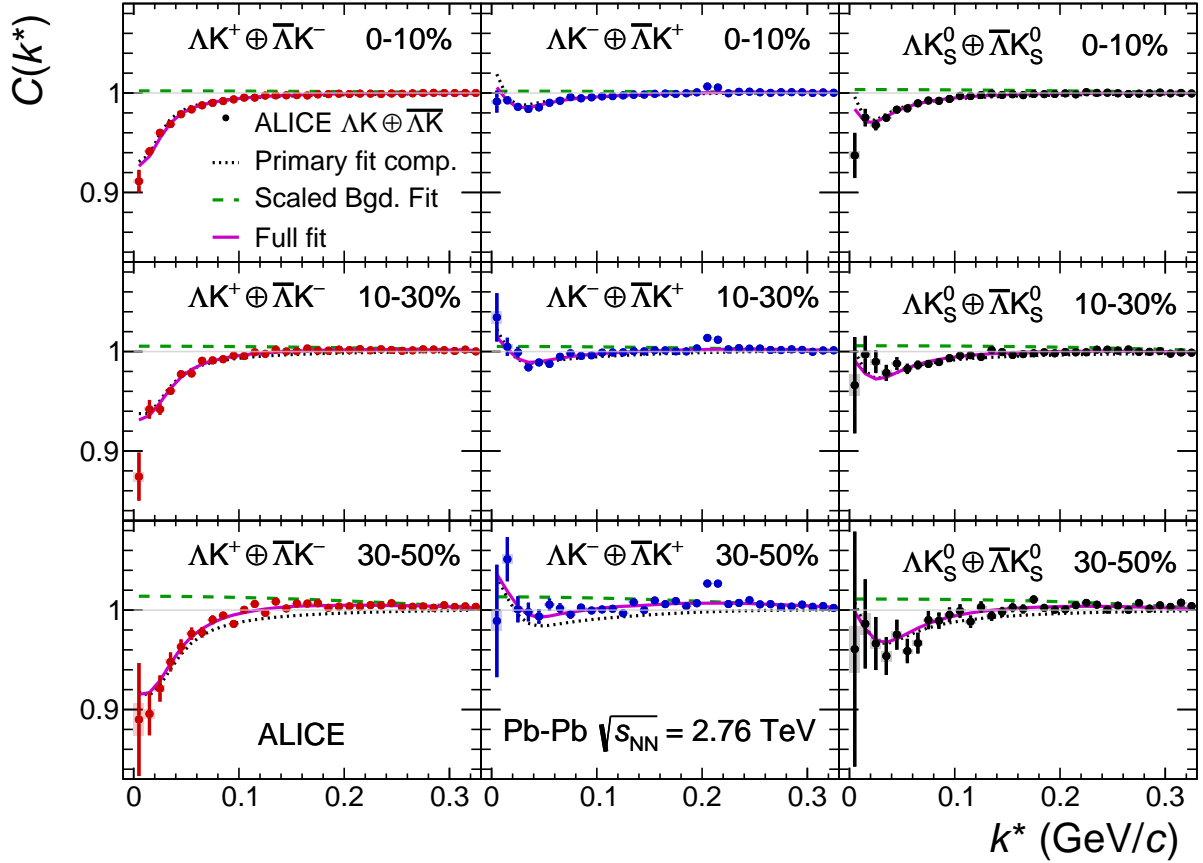


**Figure 3:** (Color online) Fit results for the  $\Lambda K$  data, with pair and conjugate combined. The  $\Lambda K^+ \oplus \bar{\Lambda} K^-$  data are shown in the left column, the  $\Lambda K^- \oplus \bar{\Lambda} K^+$  in the middle, and the  $\Lambda K_S^0 \oplus \bar{\Lambda} K_S^0$  in the right. Rows differentiate the different centrality intervals (0–10% in the top, 10–30% in the middle, and 30–50% in the bottom). Lines represent statistical uncertainties, while boxes represent systematic uncertainties. The dotted curve shows the primary ( $\Lambda K$ ) contribution to the fit, the dashed curve shows the fit to the non-femtoscopic background, and the solid curve shows the final fit.

$K_S^0$  is a mixture of the neutral  $K^0$  and  $\bar{K}^0$  states with quark content  $\frac{1}{\sqrt{2}} [\bar{d}s + \bar{s}d]$ . It is interesting to note the presence of a  $s\bar{s}$  pair in the  $\Lambda K^+$  system contrasted with a  $u\bar{u}$  pair in the  $\Lambda K^-$  system. Additionally, although the  $K_S^0$  is an average of  $K^+$  and  $K^-$  in some respects (e.g., electrically), it contains (anti)down quarks, whereas the  $K^\pm$  contain (anti)up quarks.

Figure 4 (right) presents the  $\lambda_{\text{Fit}}$  and radius parameters for all three studied centrality percentile ranges. The  $\lambda_{\text{Fit}}$  parameters are expected to be close to unity. A comparison of the extracted radii from this study to those of other systems measured by ALICE [33] is shown in Fig. 5. The figure shows  $R_{\text{inv}}$  as a function of  $m_T$  for several centrality ranges and for several different pair systems. The  $m_T$  value used for the present  $\Lambda K$  results was taken as the average of the three systems. For non-identical particle pairs, to be more directly analogous to the single particle  $m_T$ , the definition of the pair transverse mass used in this study is

$$m_{T,\text{pair}}^2 = \left( \frac{m_{\text{inv}}}{2} \right)^2 + \left( \frac{1}{2} |\mathbf{p}_{T,1} + \mathbf{p}_{T,2}| \right)^2 = (K^0)^2 - (K^3)^2, \quad \text{where } K^\mu \equiv \frac{1}{2} (p_1^\mu + p_2^\mu). \quad (14)$$

The radii are observed to increase for more central events, as expected from a simple geometric picture of the collisions. For each pair system, the radii decrease with increasing  $m_T$ , as expected in the presence of collective radial flow [4]. It was found that [34], even in the presence of global  $m_T$ -scaling for the three-dimensional radii in the Longitudinally Co-Moving System (LCMS), a particle species dependence will

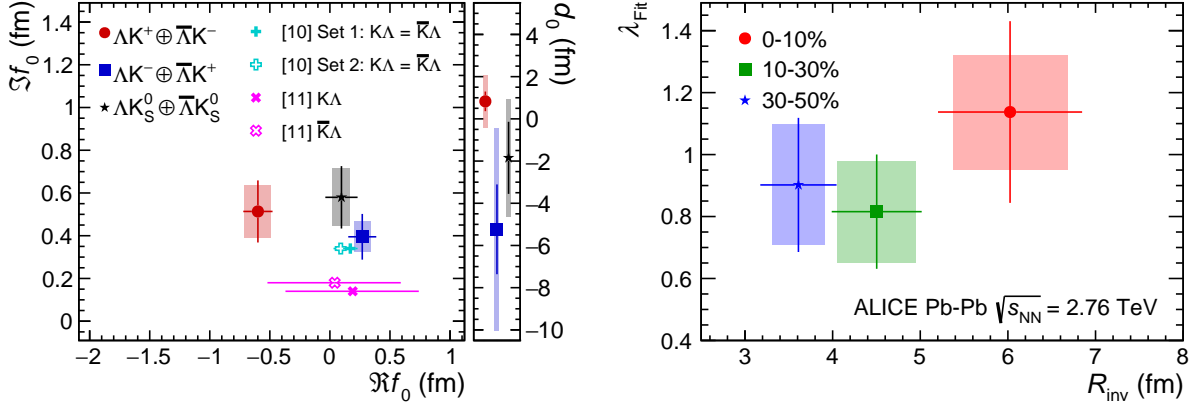


**Figure 4:** (Color online) Extracted fit parameters for all of the  $\Lambda K$  systems. (Left) The scattering parameters,  $S f_0$  and  $R f_0$ , together with  $d_0$  to the right, for the  $\Lambda K^+$  (circles),  $\Lambda K^-$  (squares) and  $\Lambda K_S^0$  (stars) systems. (Right) The  $\lambda_{\text{fit}}$  and radius parameters for the 0–10% (circles), 10–30% (squares), and 30–50% (stars) centrality intervals. In the fit, all  $\Lambda K$  systems share common radii. The cross [10] and X [11] points show theoretical predictions made using chiral perturbation theory.

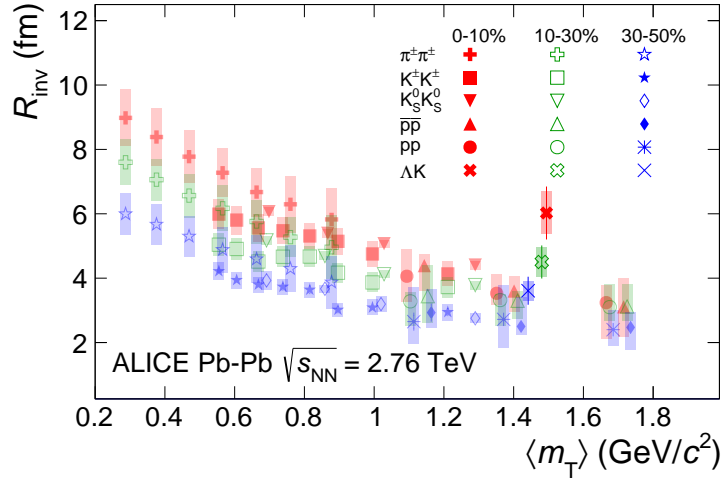


**Figure 5:** (Color online) Extracted fit  $R_{\text{inv}}$  parameters as a function of pair transverse mass ( $m_T$ ) for several centralities. Results from the  $\Lambda K$  analysis are presented together with ALICE published data [33] for various other pair systems.

exist for the  $R_{\text{inv}}$  measured in the PRF, due to trivial kinematic reasons. These kinematic effects, resulting from the transformation from LCMS to PRF, cause smaller masses to exhibit larger  $R_{\text{inv}}$  [33] (explaining, for instance, why the pion radii are systematically higher than kaon radii at the same approximate  $m_T$ ).

It is clear from the results in Fig. 5 that the  $\Lambda K$  systems do not conform to the approximate  $m_T$ -scaling of the identical particle pair source sizes. There are two important consequences of the hydrodynamic nature of the system to consider when interpreting non-identical femtoscopic results. First, the hydrodynamic response of the medium produces the approximate  $m_T$ -scaling with respect to the single-particle sources. Second, this response confines higher- $m_T$  particles to smaller homogeneity regions and pushes their average emission points further in the “out” direction [5] in a coordinate system chosen according to the out-side-long prescription (where the “long” axis is parallel to the beam, “out” is parallel to the total transverse momentum of the pair, and “side” is orthogonal to both). For identical particle studies, in which the pair source is comprised of two identical single particle sources commonly affected by the space-time shift, the femtoscopic radii naturally follow the  $m_T$ -scaling trend. However, for the case of non-identical particles, the pair emission source is a superposition of two unique single-particle sources,



which are affected differently by the hydrodynamic response of the system. Therefore, the  $\Lambda$  and K sources differ both in size and space–time location, leading to an “emission asymmetry”, with the  $\Lambda$  source both smaller in size and further out in the fireball than that of the kaons.

A separation of the single-particle sources in the “out” direction is expected for  $\Lambda$ K pairs at mid-rapidity in Pb–Pb collisions, as described above, and the experimental data support such an emission asymmetry. In addition to the “size” of the emitting region (more precisely, the second moments of the emission functions) accessible with identical particle studies, non-identical particle correlations are sensitive to the relative emission shifts, i.e., the first moments of the emission function [6]. The spherical harmonic decomposition of the correlation function offers an elegant method for extracting information about the emission asymmetries [35–37]. With this method, one can draw a wealth of information from just a few components of the decomposition. Particularly, the  $l = 0, m = 0$  component,  $C_{00}$ , quantifies the angle-integrated strength of the correlation function, and probes the overall size of the source. Of interest here, the real part of the  $l = 1, m = 1$  component,  $\Re C_{11}$ , probes the asymmetry of the system in the “out” direction; a non-zero value reveals the asymmetry. Figure 6 shows the  $C_{00}$  and  $\Re C_{11}$  components from the spherical decomposition of the  $\Lambda K^+$  data in the 0–10% centrality interval. The  $\Re C_{11}$  component shows a clear deviation from zero, and the negative value signifies that the  $\Lambda$  particles are, on average, emitted further out and/or earlier than the K mesons. This conclusion is supported by the results obtained from the THERMINATOR 2 model, shown in Fig. C.1. Furthermore, this emission asymmetry effect can inflate the radii extracted with the one-dimensional Lednický model, which assumes a spherically symmetric source with no offsets (i.e.,  $R_{\text{out}} = R_{\text{side}} = R_{\text{long}}$  and  $\mu_{\text{out}} = \mu_{\text{side}} = \mu_{\text{long}} = 0$ ). This effect is demonstrated in Appendix C using the THERMINATOR 2 simulation. In Fig. 5, the largest violation of the  $m_T$ -scaling for the  $\Lambda K$  system is observed for the 0–10% centrality interval, in which one expects the largest emission asymmetry.

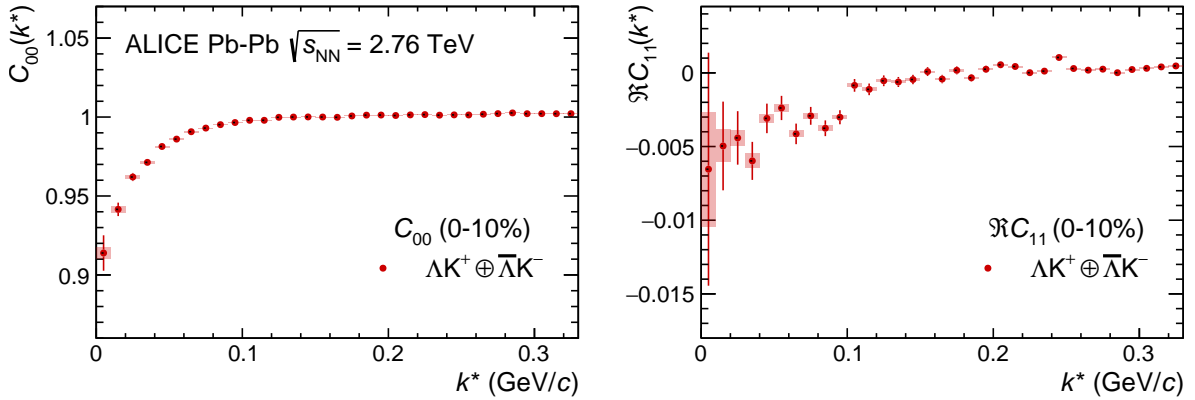


**Figure 6:** (Color online) Spherical harmonics components  $C_{00}$  (left) and  $\Re C_{11}$  (right) of the  $\Lambda K^+$  correlation function for the 0–10% centrality interval. The  $C_{00}$  component is similar to the one-dimensional correlation functions typically studied, and probes the overall size of the source. The  $\Re C_{11}$  component probes the asymmetry in the system; a non-zero value reveals the asymmetry.

## 5 Summary

Results from a femtoscopic analysis of  $\Lambda K$  correlations in Pb–Pb collisions at  $\sqrt{s_{\text{NN}}} = 2.76$  TeV measured by the ALICE experiment at the LHC have been presented, and are summarized in Table 5. The femtoscopic radii,  $\lambda$  parameters, and scattering parameters were extracted from one-dimensional correlation functions in terms of the invariant momentum difference. The scattering parameters of  $\Lambda K$  pairs in all three charge combinations ( $\Lambda K^+$ ,  $\Lambda K^-$ , and  $\Lambda K_S^0$ ) were measured for the first time. The non-femtoscopic backgrounds observed in the experimental data were described quantitatively with the THERMINATOR 2 event generator, and were found to result almost entirely from collective effects.

**Table 5:** Extracted fit parameters. The uncertainties marked as “stat.” are those returned by MINUIT, and those marked as “syst.” result from the systematic analysis.

Centrality	$\lambda_{\text{Fit}}$	$R_{\text{inv}}$
0–10%	$1.14 \pm 0.29 \text{ (stat.)} \pm 0.18 \text{ (syst.)}$	$6.02 \pm 0.82 \text{ (stat.)} \pm 0.65 \text{ (syst.)}$
10–30%	$0.82 \pm 0.18 \text{ (stat.)} \pm 0.16 \text{ (syst.)}$	$4.50 \pm 0.51 \text{ (stat.)} \pm 0.45 \text{ (syst.)}$
30–50%	$0.90 \pm 0.22 \text{ (stat.)} \pm 0.19 \text{ (syst.)}$	$3.61 \pm 0.44 \text{ (stat.)} \pm 0.30 \text{ (syst.)}$

System	$\Re f_0$	$\Im f_0$	$d_0$
$\Lambda K^+ \oplus \bar{\Lambda} K^-$	$-0.60 \pm 0.12 \text{ (stat.)} \pm 0.11 \text{ (syst.)}$	$0.51 \pm 0.15 \text{ (stat.)} \pm 0.12 \text{ (syst.)}$	$0.83 \pm 0.47 \text{ (stat.)} \pm 1.23 \text{ (syst.)}$
$\Lambda K^- \oplus \bar{\Lambda} K^+$	$0.27 \pm 0.12 \text{ (stat.)} \pm 0.07 \text{ (syst.)}$	$0.40 \pm 0.11 \text{ (stat.)} \pm 0.07 \text{ (syst.)}$	$-5.23 \pm 2.13 \text{ (stat.)} \pm 4.80 \text{ (syst.)}$
$\Lambda K_S^0 \oplus \bar{\Lambda} K_S^0$	$0.10 \pm 0.13 \text{ (stat.)} \pm 0.07 \text{ (syst.)}$	$0.58 \pm 0.15 \text{ (stat.)} \pm 0.13 \text{ (syst.)}$	$-1.85 \pm 1.71 \text{ (stat.)} \pm 2.77 \text{ (syst.)}$

Striking differences are observed in the  $\Lambda K^+$ ,  $\Lambda K^-$ , and  $\Lambda K_S^0$  correlation functions, which are reflected in the unique set of scattering parameters extracted for each. These scattering parameters indicate that the strong force is repulsive in the  $\Lambda K^+$  interaction and attractive in the  $\Lambda K^-$  and  $\Lambda K_S^0$  interactions. This effect could be due to different quark–antiquark interactions between the pairs, or from different net strangeness present in each system. The extracted source radii describing the  $\Lambda K$  systems are larger than expected from naive extrapolation of identical particle femtoscopic studies. This effect is interpreted as resulting from the separation in space–time of the single-particle  $\Lambda$  and  $K$  source distributions (i.e., the emission asymmetry of the source), which is confirmed by the spherical harmonics decomposition of the correlation functions.

## Acknowledgements

## References

- [1] M. A. Lisa, S. Pratt, R. Soltz, and U. Wiedemann, “Femtoscopy in relativistic heavy ion collisions”, *Ann. Rev. Nucl. Part. Sci.* **55** (2005), arXiv:nucl-ex/0505014 [nucl-ex].
- [2] M. A. Lisa and S. Pratt, “Femtoscopically Probing the Freeze-out Configuration in Heavy Ion Collisions”, in *Relativistic Heavy Ion Physics*, R. Stock, ed. 2010. arXiv:0811.1352 [nucl-ex].
- [3] A. N. Makhlin and Yu. M. Sinyukov, “Hydrodynamics of Hadron Matter Under Pion Interferometric Microscope”, *Z. Phys. C* **39** (1988) . [,238(1987)].
- [4] S. V. Akkelin and Yu. M. Sinyukov, “The HBT interferometry of expanding sources”, *Phys. Lett. B* **356** (1995) .
- [5] F. Retiere and M. A. Lisa, “Observable implications of geometrical and dynamical aspects of freeze out in heavy ion collisions”, *Phys. Rev. C* **70** (2004), arXiv:nucl-th/0312024 [nucl-th].
- [6] A. Kisiel, “Non-identical particle femtoscopy at  $\sqrt{s_{\text{NN}}} = 200$  GeV in hydrodynamics with statistical hadronization”, *Phys. Rev. C* **81** (2010), arXiv:0909.5349 [nucl-th].
- [7] R. Lednicky, V. L. Lyuboshits, B. Erasmus, and D. Nouais, “How to measure which sort of particles was emitted earlier and which later”, *Phys. Lett. B* **373** (1996) .
- [8] S. Voloshin, R. Lednicky, S. Panitkin, and N. Xu, “Relative space-time asymmetries in pion and nucleon production in noncentral nucleus-nucleus collisions at high-energies”, *Phys. Rev. Lett.* **79** (1997), arXiv:nucl-th/9708044 [nucl-th].

- [9] R. Lednicky, “Femtoscopy with unlike particles”, in *International Workshop on the Physics of the Quark Gluon Plasma Palaiseau, France, September 4-7, 2001*. 2001. arXiv:nucl-th/0112011 [nucl-th].
- [10] Y.-R. Liu and S.-L. Zhu, “Meson-baryon scattering lengths in HB $\chi$ PT”, *Phys. Rev. D* **75** (2007), arXiv:hep-ph/0607100 [hep-ph].
- [11] M. Mai, P. C. Bruns, B. Kubis, and U.-G. Meissner, “Aspects of meson-baryon scattering in three and two-flavor chiral perturbation theory”, *Phys. Rev. D* **80** (2009), arXiv:0905.2810 [hep-ph].
- [12] W. E. Humphrey and R. R. Ross, “Low-Energy Interactions of K- Mesons in Hydrogen”, *Phys. Rev.* **127** (1962) .
- [13] D. Hadjimichief, J. Haidenbauer, and G. Krein, “Short range repulsion and isospin dependence in the KN system”, *Phys. Rev. C* **66** (2002), arXiv:nucl-th/0209026 [nucl-th].
- [14] Y. Ikeda, T. Hyodo, and W. Weise, “Chiral SU(3) theory of antikaon-nucleon interactions with improved threshold constraints”, *Nucl. Phys. A* **881** (2012), arXiv:1201.6549 [nucl-th].
- [15] R. Lednický and V. L. Lyuboshitz, “Final State Interaction Effect on Pairing Correlations Between Particles with Small Relative Momenta”, *Sov. J. Nucl. Phys.* **35** (1982) . [Yad. Fiz.35,1316 (1981)].
- [16] ALICE Collaboration, K. Aamodt *et al.*, “The ALICE experiment at the CERN LHC”, *JINST* **3** (2008) .
- [17] ALICE Collaboration, B. Abelev *et al.*, “Centrality determination of Pb-Pb collisions at  $\sqrt{s_{NN}} = 2.76$  TeV with ALICE”, *Phys. Rev. C* **88** no. 4, (2013), arXiv:1301.4361 [nucl-ex].
- [18] J. Alme *et al.*, “The ALICE TPC, a large 3-dimensional tracking device with fast readout for ultra-high multiplicity events”, *Nucl. Instrum. Meth. A* **622** (2010), arXiv:1001.1950 [physics.ins-det].
- [19] ALICE Collaboration, B. Abelev *et al.*, “Technical Design Report for the Upgrade of the ALICE Inner Tracking System”, *J. Phys. G* **41** (2014) .
- [20] ALICE Collaboration, B. B. Abelev *et al.*, “Performance of the ALICE Experiment at the CERN LHC”, *Int. J. Mod. Phys. A* **29** (2014), arXiv:1402.4476 [nucl-ex].
- [21] A. Akindinov *et al.*, “Performance of the ALICE Time-Of-Flight detector at the LHC”, *Eur. Phys. J. Plus* **128** (2013) .
- [22] X.-N. Wang and M. Gyulassy, “HIJING: A Monte Carlo model for multiple jet production in pp, pA, and AA collisions”, *Phys. Rev. D* **44** (Dec, 1991) .  
<https://link.aps.org/doi/10.1103/PhysRevD.44.3501>.
- [23] R. Brun, F. Bruyant, F. Carminati, S. Giani, M. Maire, A. McPherson, G. Patrick, and L. Urban, *GEANT: Detector Description and Simulation Tool; Oct 1994*. CERN Program Library. CERN, Geneva, 1993. <https://cds.cern.ch/record/1082634>. Long Writeup W5013.
- [24] ALICE Collaboration, S. Acharya *et al.*, “Kaon femtoscopy in Pb-Pb collisions at  $\sqrt{s_{NN}} = 2.76$  TeV”, *Phys. Rev. C* **96** no. 6, (2017), arXiv:1709.01731 [nucl-ex].
- [25] Particle Data Group Collaboration, M. Tanabashi *et al.*, “Review of particle physics”, *Phys. Rev. D* **98** (Aug, 2018) . <https://link.aps.org/doi/10.1103/PhysRevD.98.030001>.

- [26] S. E. Koonin, “Proton Pictures of High-Energy Nuclear Collisions”, *Phys. Lett. B* **70** (1977) .
- [27] S. Pratt, T. Csorgo, and J. Zimanyi, “Detailed predictions for two pion correlations in ultrarelativistic heavy ion collisions”, *Phys. Rev. C* **42** (1990) .
- [28] G. I. Kopylov, “Like particle correlations as a tool to study the multiple production mechanism”, *Phys. Lett. B* **50** (1974) .
- [29] A. Kisiel, H. Zbroszczyk, and M. Szymaski, “Extracting baryon-antibaryon strong interaction potentials from  $p\bar{\Lambda}$  femtoscopic correlation functions”, *Phys. Rev. C* **89** no. 5, (2014) , arXiv:1403.0433 [nucl-th].
- [30] ALICE Collaboration, S. Acharya *et al.*, “p-p, p- $\Lambda$  and  $\Lambda$ - $\Lambda$  correlations studied via femtoscopy in pp reactions at  $\sqrt{s} = 7$  TeV”, *Phys. Rev. C* **99** no. 2, (2019) , arXiv:1805.12455 [nucl-ex].
- [31] M. Chojnacki, A. Kisiel, W. Florkowski, and W. Broniowski, “THERMINATOR 2: THERMal heavy IoN generATOR 2”, *Comput. Phys. Commun.* **183** (2012) , arXiv:1102.0273 [nucl-th].
- [32] A. Kisiel, “Non-identical particle correlation analysis in the presence of non-femtoscopic correlations”, *Acta Physica Polonica B* **48** (04, 2017) .
- [33] ALICE Collaboration, J. Adam *et al.*, “One-dimensional pion, kaon, and proton femtoscopy in Pb-Pb collisions at  $\sqrt{s_{NN}} = 2.76$  TeV”, *Phys. Rev. C* **92** no. 5, (2015) , arXiv:1506.07884 [nucl-ex].
- [34] A. Kisiel, M. Gaayn, and P. Boek, “Pion, kaon, and proton femtoscopy in Pb–Pb collisions at  $\sqrt{s_{NN}} = 2.76$  TeV modeled in (3+1)D hydrodynamics”, *Phys. Rev. C* **90** no. 6, (2014) , arXiv:1409.4571 [nucl-th].
- [35] Z. Chajecki and M. Lisa, “Global Conservation Laws and Femtoscopy of Small Systems”, *Phys. Rev. C* **78** (2008) , arXiv:0803.0022 [nucl-th].
- [36] D. A. Brown, A. Enokizono, M. Heffner, R. Soltz, P. Danielewicz, and S. Pratt, “Imaging three dimensional two-particle correlations for heavy-ion reaction studies”, *Phys. Rev. C* **72** (Nov, 2005) . <https://link.aps.org/doi/10.1103/PhysRevC.72.054902>.
- [37] A. Kisiel and D. A. Brown, “Efficient and robust calculation of femtoscopic correlation functions in spherical harmonics directly from the raw pairs measured in heavy-ion collisions”, *Phys. Rev. C* **80** (2009) , arXiv:0901.3527 [nucl-th].
- [38] A. Stavinskiy *et al.*, “Some new aspects of femtoscopy at high energy”, *Nukleonika* **49** (Supplement 2) (2004) . [http://www.nukleonika.pl/www/back/full/vol49\\_2004/v49s2p023f.pdf](http://www.nukleonika.pl/www/back/full/vol49_2004/v49s2p023f.pdf).
- [39] ALICE Collaboration, K. Aamodt *et al.*, “Two-pion Bose-Einstein correlations in central Pb-Pb collisions at  $\sqrt{s_{NN}} = 2.76$  TeV”, *Phys. Lett. B* **696** (2011) , arXiv:1012.4035 [nucl-ex].
- [40] R. Lednický, “Finite-size effects on two-particle production in continuous and discrete spectrum”, *Phys. Part. Nucl.* **40** (2009) , arXiv:nucl-th/0501065 [nucl-th].

## A Stavinskiy reference method

Another option for obtaining the reference distribution,  $B(k^*)$ , is to use, what will be referred to as, the “Stavinskiy method” [38]. The method was first proposed to handle the case of one event femtoscopy, and has been suggested for use in eliminating momentum conservation effects in the reference distribution [1]. The method is appropriate for collisions between symmetric projectiles, at sufficiently large energy, with a detector which is symmetrical with respect to the transformation  $\mathbf{r} \rightarrow -\mathbf{r}$ . The use of this method in a three-dimensional analysis of two-pion correlations produced, in comparison to the event mixing results, an increase of 6% for  $R_{\text{side}}$  at low- $k_T$  and up to 4% for  $R_{\text{out}}$  and  $R_{\text{long}}$  [39]. The purpose of using the Stavinskiy method in this  $\Lambda K$  analysis is to rid the correlation functions of the non-femtoscopic background. More specifically, the intent is to handle background contributions from elliptic flow, and other sources having reflection symmetry in the transverse plane. With the Stavinskiy method, mixed-event pairs are not used for the reference distribution; instead, same-event pseudo-pairs, formed by rotating one particle in a real pair by  $180^\circ$  in the transverse plane, are used. This rotation rids the pairs of any femtoscopic correlation, while maintaining correlations due to elliptic flow (and other suitably symmetric contributors). Care needs to be taken in treating the pseudo-pairs exactly like the real pairs; e.g., the pseudo-pairs should be exposed to the same pair rejection procedures used in the analysis on the real pairs. The results of correctly implementing such a procedure are shown in Fig. A.1. The figure demonstrates, for the  $\Lambda K^+$  system, that the Stavinskiy method is effective in flattening the correlation function in the region where no femtoscopic signal is expected.

## B Strong and Coulomb fitter

When modeling systems which include both strong and Coulomb effects, Eq. (5) is no longer valid, and there exists no analytical form with which to fit. To model such a system, a more fundamental approach must be taken, beginning with Eq. (2) and using the two-particle wave-function which includes both strong and Coulomb interactions [40],

$$\Psi_{\mathbf{k}^*}(\mathbf{r}^*) = e^{i\delta_c} \sqrt{A_c(\eta)} [e^{i\mathbf{k}^* \cdot \mathbf{r}^*} F(-i\eta, 1, i\xi) + f_c(k^*) \frac{\tilde{G}(\rho, \eta)}{r^*}], \quad (\text{B.1})$$

where  $\rho = k^* r^*$ ,  $\eta = (k^* a_c)^{-1}$ ,  $\xi = \mathbf{k}^* \cdot \mathbf{r}^* + k^* r^* \equiv \rho(1 + \cos \theta^*)$ , and  $a_c = (\mu z_1 z_2 e^2)^{-1}$  is the two-particle Bohr radius (including the sign of the interaction). Furthermore,  $\delta_c$  is the Coulomb s-wave phase shift,  $A_c(\eta)$  is the Coulomb penetration factor,  $\tilde{G} = \sqrt{A_c}(G_0 + iF_0)$  is a combination of the regular ( $F_0$ ) and singular ( $G_0$ ) s-wave Coulomb functions. Finally,  $f_c(k^*)$  is the s-wave scattering amplitude,

$$f_c(k^*) = \left[ \frac{1}{f_0} + \frac{1}{2} d_0 k^{*2} - \frac{2}{a_c} h(\eta) - i k^* A_c(\eta) \right]^{-1}, \quad (\text{B.2})$$

where the “h-function”,  $h(\eta)$ , is expressed through the digamma function,  $\psi(z) = \Gamma'(z)/\Gamma(z)$  as

$$h(\eta) = 0.5[\psi(i\eta) + \psi(-i\eta) - \ln(\eta^2)]. \quad (\text{B.3})$$

In this case, the  $\lambda$  parameter may be included as

$$C(\mathbf{k}^*) = (1 - \lambda) + \lambda \int S(\mathbf{r}^*) |\Psi_{\mathbf{k}^*}^S(\mathbf{r}^*)|^2 d^3 \mathbf{r}^*. \quad (\text{B.4})$$

To build a fit function for a system including both strong and Coulomb interactions two related options were considered. The first option was to numerically integrate Eq. (2). The second option was to simulate a large sample of particle pairs, calculate the wave function describing the interaction, and average to obtain the integral in Eq. (2). For this analysis, the latter option was adopted.

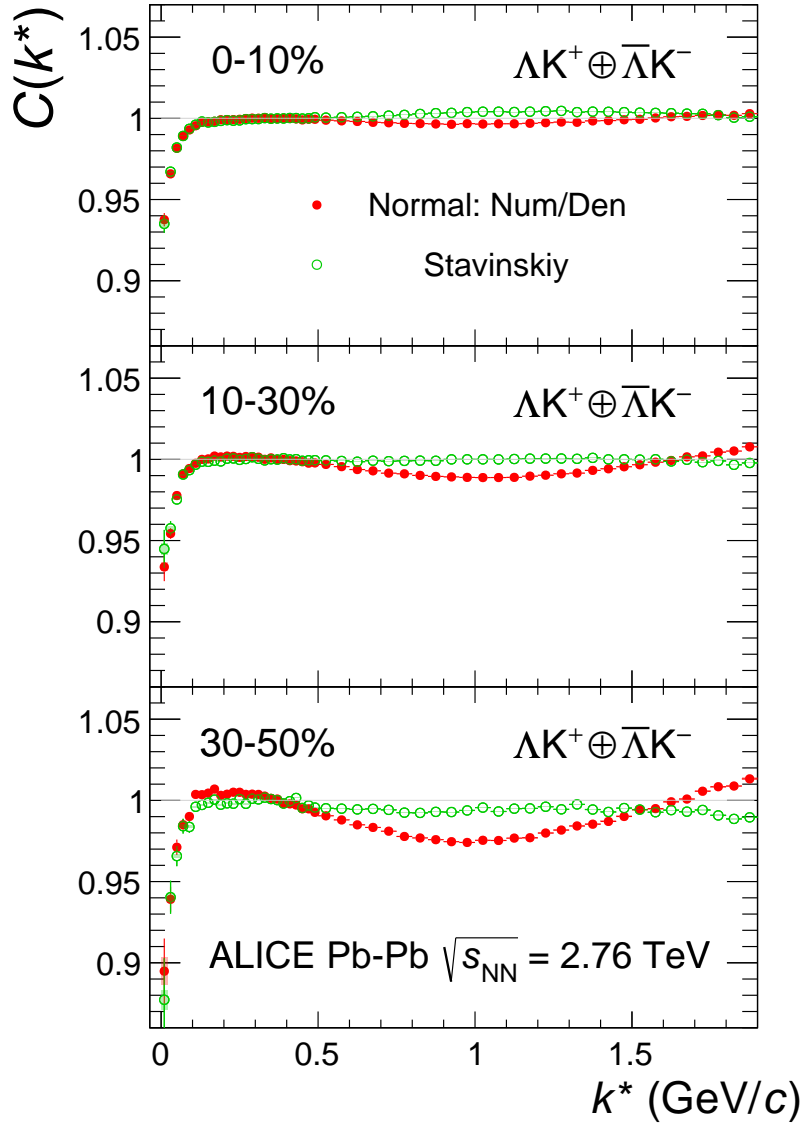


**Figure A.1:** (Color online) Correlation functions for the  $\Lambda K^+ \oplus \bar{\Lambda} K^-$  system built using the Stavinskiy method for 0–10%, 10–30%, and 30–50% centrality intervals. Closed symbols represent correlations built using the normal mixed-event reference distribution, while open symbols represent correlations formed using the Stavinskiy same-event pseudo-pairs as a reference.

## C Relative emission shifts with THERMINATOR 2

Figure C.1 shows  $\Lambda K^+$  results from the THERMINATOR 2 event generator for an impact parameter of  $b = 2$  fm. As THERMINATOR 2 does not include any final state effects, the femtosopic correlation was introduced by assuming a set of scattering parameters  $(\Re f_0, \Im f_0, d_0) = (-0.60 \text{ fm}, 0.51 \text{ fm}, 0.83 \text{ fm})$  and weighting the pairs in the signal distribution with the modulus squared of the two-particle wave function,  $|\Psi|^2$ .

The top row of Fig. C.1 shows the experimental  $\Lambda K^+ \oplus \bar{\Lambda} K^-$  data together with the simulation results (a) for the one-dimensional correlation function and (b) for the real part of the  $l = 1, m = 1$  component,  $\Re C_{11}$ , of the spherical harmonic decomposition. The other four plots in Fig. C.1 show the two-particle emission function (i.e., the pair separation distributions) from the simulation in the (c) out ( $r_{\text{out}}^*$ ), (d) side ( $r_{\text{side}}^*$ ), and (e) long ( $r_{\text{long}}^*$ ) directions, as well as (f) the temporal characteristics of the source ( $\Delta t^*$ ), all

measured in the PRF. The source distributions have all been fitted with a Gaussian form, the results of which are printed within the respective plots. One immediately sees a significant spatial shift in the out direction,  $\mu_{\text{out}} \approx 4$  fm, and negligible shift in the other two directions,  $\mu_{\text{side}} \approx \mu_{\text{long}} \approx 0$  fm. In other words, the figure demonstrates that, within the THERMINATOR 2 model, the  $\Lambda$  is, on average, emitted further out than its K partner. Additionally, the figure shows a nonzero temporal shift,  $\mu_{\Delta t} \approx -2.7$  fm/c, signifying that the  $\Lambda$  is, on average, emitted earlier than its K partner within the model.

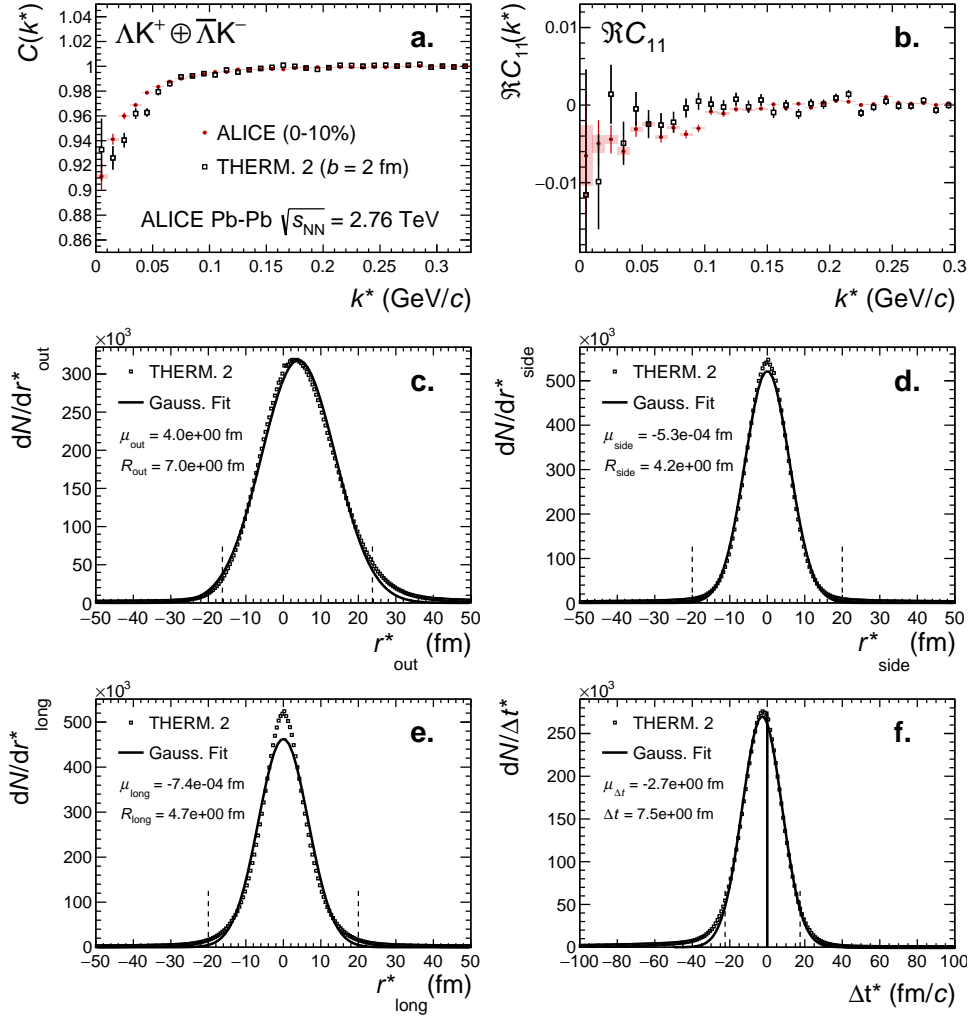


**Figure C.1:** Results from the THERMINATOR 2 simulation implemented with an impact parameter  $b = 2$  fm for the  $\Lambda K^+$  pair system. (a) the one-dimensional correlation function from THERMINATOR 2 together with the experimental data. (b) the  $\Re C_{11}$  component of a spherical harmonic decomposition of the THERMINATOR 2 simulation together with the experimental data. The other four panels show the source distribution from the simulation in the (c) out, (d) side, and (e) long directions, as well as (f) the temporal characteristics, all in the PRF. The source distributions have all been fitted with a Gaussian form over the regions contained within the dashed lines, the results of which are printed within the respective plots.

This section concludes with a brief look at how a spatial separation of the single particle sources affects the radii extracted from a femtoscopic analysis. To achieve this, THERMINATOR 2 is used in a similar fashion as described above, but with one important difference. Instead of taking the source information from THERMINATOR 2, the source is drawn from a pre-determined Gaussian distribution. In all,  $R_{\text{out}} = R_{\text{side}} = R_{\text{long}} = 5$  fm, and  $\mu_{\text{side}} = \mu_{\text{long}} = 0$  fm. The cases of  $\mu_{\text{out}} = 0$  fm,  $\mu_{\text{out}} = 1$  fm,  $\mu_{\text{out}} = 3$  fm, and  $\mu_{\text{out}} = 6$  fm were studied within the simulation. Note, within this implementation there is no time difference in the emission of the  $\Lambda$  and K particles. For each, a one-dimensional correlation function is generated and

fit with the Lednický model, as shown in Fig. C.2. The scattering parameters are known precisely here, as they served as the weights used in the simulation, and are kept constant in the fit. Only the extracted one-dimensional source size is of interest here, so the  $\lambda$  parameter is also fixed at unity. The figure demonstrates that as the separation  $\mu_{\text{out}}$  increases, so do the extracted femtoscopic radii. Figure C.3 shows, together with the experimental  $\Lambda K^+$  data, the effect of increasing  $\mu_{\text{out}}$  on the spherical harmonic  $l = 0, m = 0$  component,  $C_{00}$ , and on the real part of the  $l = 1, m = 1$  component,  $\Re C_{11}$ . The figures shows that as  $\mu_{\text{out}}$  increases, so does the magnitude of the  $\Re C_{11}$  signal.

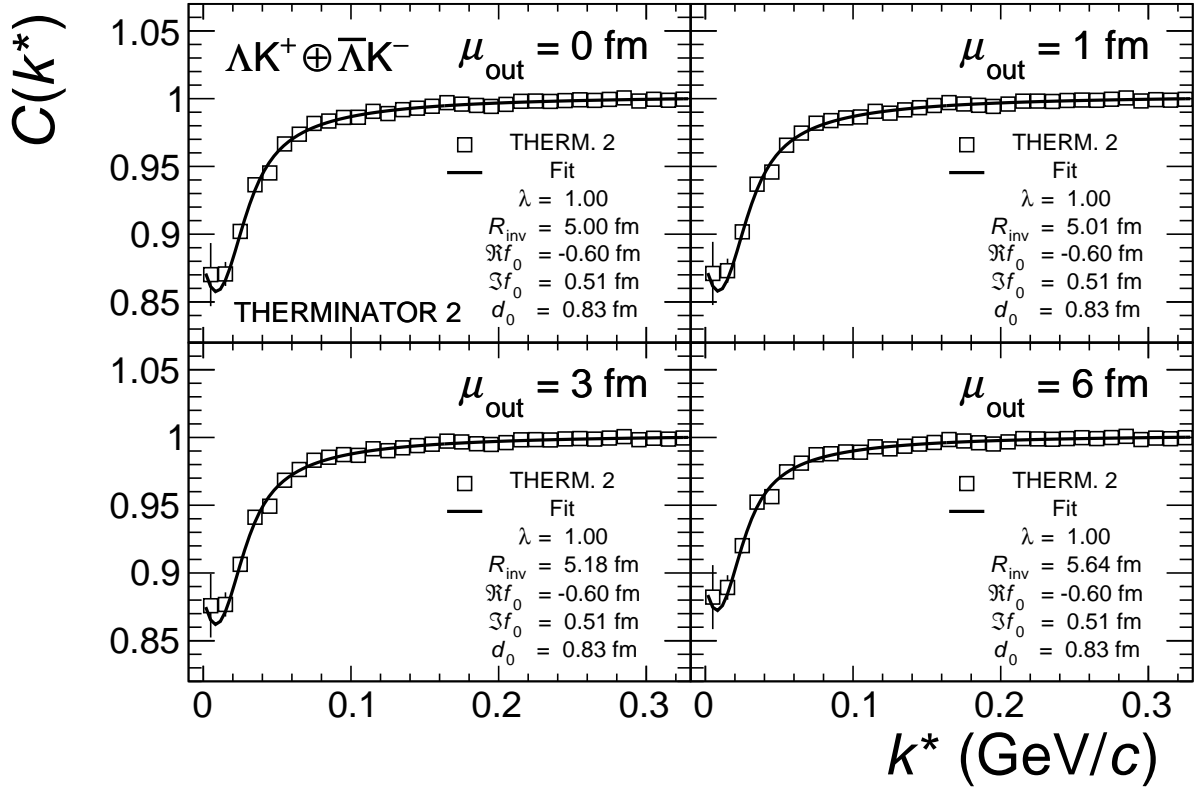


**Figure C.2:** Probing the effect of varying the source shift in the outward direction,  $\mu_{\text{out}}$ , within the THERMINATOR 2 framework. To achieve this, particle pairs are formed from the simulation, but with altered spatial characteristics achieved by drawing the out, side, and long components from predetermined Gaussian distributions. The sources in all three directions are Gaussians of width 5 fm. The distributions used for the side and long direction are centered at the origin, while the shift in the outward direction,  $\mu_{\text{out}}$ , is varied. The plots show fits resulting from sources with  $\mu_{\text{out}}$  increasing from 0 to 6 fm. The effect of increasing  $\mu_{\text{out}}$  clearly increases the effective radius extracted in the fit.



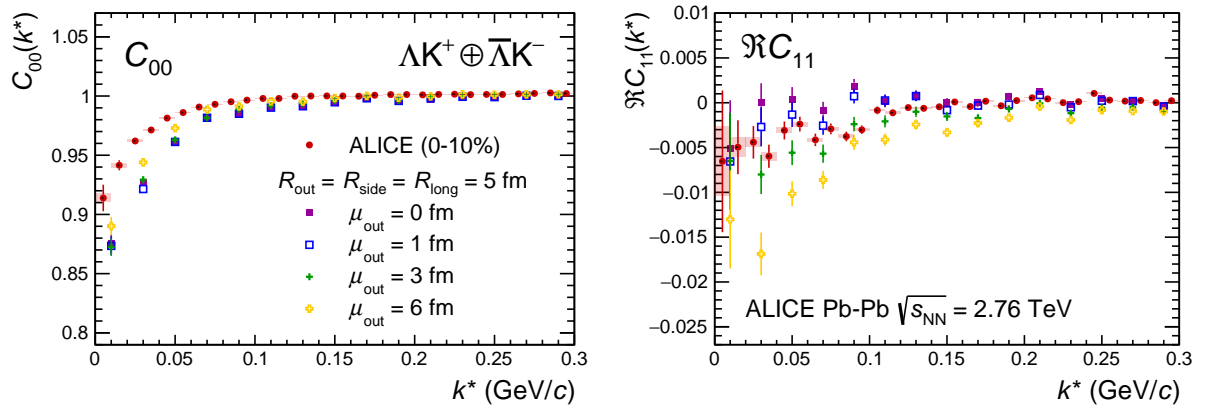


**Figure C.3:** (Color online) Spherical harmonics components (left)  $C_{00}$  and (right)  $\Re C_{11}$  of the  $\Lambda K^+$  correlation function for the 0–10% centrality interval shown with results from the THERMINATOR 2 simulation implemented with different shifts in the outward direction,  $\mu_{\text{out}}$ , as described in the text.

644 **D The ALICE Collaboration**